

Frictional and hydrologic properties of clay-rich fault gouge

Matt J. Ikari,¹ Demian M. Saffer,¹ and Chris Marone¹

Received 9 September 2008; revised 11 February 2009; accepted 10 March 2009; published 19 May 2009.

[1] The slip behavior of major faults depends largely on the frictional and hydrologic properties of fault gouge. We report on laboratory experiments designed to measure the strength, friction constitutive properties, and permeability of a suite of saturated clay-rich fault gouges, including: a 50:50% mixture of montmorillonite-quartz, powdered illite shale, and powdered chlorite schist. Friction measurements indicate that clay-rich gouges are consistently weak, with steady state coefficient of sliding friction of <0.35 . The montmorillonite gouge ($\mu = 0.19\text{--}0.23$) is consistently weaker than the illite and chlorite gouges ($\mu = 0.27\text{--}0.32$). At effective normal stresses from 12 to 59 MPa, all gouges show velocity-strengthening frictional behavior in the sliding velocity range $0.5\text{--}300 \mu\text{m/s}$. We suggest that the velocity-strengthening behavior we observe is related to saturation of real contact area, as documented by the friction parameter b , and is an inherent characteristic of noncohesive, unlithified clay-rich gouge. Permeability normal to the gouge layer measured before, during, and after shear ranges from $8.3 \times 10^{-21} \text{ m}^2$ to $3.6 \times 10^{-16} \text{ m}^2$; permeability decreases dramatically with shearing, and to a lesser extent with increasing effective normal stress. The chlorite gouge is consistently more permeable than the montmorillonite and illite gouge and maintains a higher permeability after shearing. Permeability reduction via shear is pronounced at shear strains $\lesssim 5$ and is smaller at higher strain, suggesting that shear-induced permeability reduction is linked to fabric development early in the deformation history. Our results imply that the potential for development of excess pore pressure in low-permeability fault gouge depends on both clay mineralogy and shear strain.

Citation: Ikari, M. J., D. M. Saffer, and C. Marone (2009), Frictional and hydrologic properties of clay-rich fault gouge, *J. Geophys. Res.*, *114*, B05409, doi:10.1029/2008JB006089.

1. Introduction

[2] Clay minerals are abundant in mature fault zones, including both subduction megathrusts and continental transform faults like the San Andreas Fault, and their properties are considered a major control on macroscopic fault behavior in the brittle crust [Vrolijk and van der Pluijm, 1999; Underwood, 2007; Numelin et al., 2007; Ikari et al., 2007]. For example, the presence of weak clay minerals is hypothesized as one mechanism to explain the overall mechanical weakness of major plate boundary faults [e.g., Wu et al., 1975; Deng and Underwood, 2001]. Increasing pressure and temperature with depth alter clay minerals via mineral transformation, dehydration, and mechanical consolidation, and the accompanying changes in fault zone lithification state and/or clay mineralogy have been proposed as an explanation for the upper transition from aseismic to seismic fault slip [Marone and Scholz, 1988; Hyndman et al., 1997; Moore and Saffer, 2001; Saffer and Marone, 2003]. Fault strength and stability may also be

affected by changes in effective normal stress and slip rate [e.g., Scholz, 1998]. In this respect, the hydrologic properties of clay-rich gouge have a significant effect on fault behavior, because low permeability gouges may act as a barrier to fluid flow, allowing the development of high pore pressures (and thus reduced effective stress) within the fault zone. In this study, we report on frictional and hydrologic properties of clay-rich fault gouge determined from confined biaxial shear experiments carried out within a newly constructed pressure vessel under true-triaxial conditions. We investigate the effects of clay mineralogy, fluid flow, sliding velocity, and effective normal stress.

[3] Many previous studies have focused on characterizing the frictional behavior of clay-rich gouge, primarily to investigate basic frictional strength [Wang and Mao, 1979; Logan and Rauenzahn, 1987; Morrow et al., 1992, 2000; Saffer and Marone, 2003; Kopf and Brown, 2003; Bourlange et al., 2004; Moore and Lockner, 2004; Ikari et al., 2007]. These studies have shown that clay contents as low as 15–20% significantly affect the strength of faults [Shimamoto and Logan, 1981] and that fault gouges dominated by clay minerals, especially montmorillonite, illite and chlorite, are frictionally weak (coefficient of friction μ : $0.03 < \mu < 0.50$) under a variety of conditions (normal stress, water content, and clay content). Less common are studies involving large strains that report detailed measurements of the transient

¹Department of Geosciences, Pennsylvania State University, University Park, Pennsylvania, USA.

and steady state frictional response to perturbations in loading velocity or strain rate. Such measurements of rate and state friction are necessary to understand the stability of frictional sliding. Systematic study of frictional constitutive properties, particularly under conditions relevant to faulting in the upper seismogenic crust, is also needed to parameterize models of rupture nucleation and propagation, including those aiming to explain thermal pressurization and slow slip events [e.g., Liu and Rice, 2005; Rice, 2006; Segall and Rice, 2006; Rubin, 2008]. Previous experiments have shown that montmorillonite and illite-rich gouges are velocity-strengthening for both subsaturated [Saffer and Marone, 2003; Ikari et al., 2007] and saturated conditions [Logan and Rauenzahn, 1987; Morrow et al., 1992; Brown et al., 2003], but have been conducted over a limited suite of experimental conditions, and the friction constitutive properties have not been comprehensively or systematically investigated.

[4] Fault gouge permeability is also an important parameter affecting fault mechanics, because low fault-normal permeability can facilitate the development of high pore fluid pressures from regional hydrologic processes, fault zone compaction, or thermal pressurization [Hubbert and Rubey, 1959; Rice, 1992; Sleep and Blanpied, 1992; Wibberley and Shimamoto, 2005; Faulkner and Rutter, 2001; Noda and Shimamoto, 2005; Segall and Rice, 2006; Bizzari and Cocco, 2006a, 2006b], leading to substantially reduced fault strength. For example, in subduction zones, low effective stress in the décollement as a result of high pore pressure is a likely control on the structure of accretionary prisms [Davis et al., 1983; Byrne and Fisher, 1990; Le Pichon et al., 1993] and possibly the updip limit of seismicity [Moore and Saffer, 2001; Wang and Hu, 2006]. High pore pressures have also been offered as an explanation for the apparent anomalous weakness of the San Andreas Fault [Byerlee, 1990; Hickman, 1991; Rice, 1992], and recent results from the SAFOD borehole suggest that the fault acts as a barrier to regional scale fluid flow [e.g., Wiersberg and Erzinger, 2007, 2008]. Previous laboratory experiments have revealed that sediments composed of at least 50% clay minerals have very low permeabilities ($\leq 10^{-18} \text{ m}^2$). These include unsheared [Kwon et al., 2004; Yang and Aplin, 2007], naturally sheared [Faulkner and Rutter, 2000, 2003], and both naturally sheared and laboratory sheared samples [Morrow et al., 1984; Zhang et al., 1999; Zhang and Cox, 2000; Takahashi et al., 2007; Crawford et al., 2008].

[5] Although many studies have assessed frictional strength and stability of fault gouge, detailed and systematic investigations of frictional constitutive behavior under conditions relevant to seismogenic faulting in the upper crust are rare. Most existing studies consider only a limited range of experimental conditions (shear strain, effective normal stress, gouge composition, saturation, or sliding velocity). Furthermore, it remains a challenge to compare results from different experimental configurations (e.g., ring shear in which samples are small and slip velocity may vary across the sample; triaxial shear where the geometry is complex, cocking may occur, jacket stretching is an issue, and shear offset is limited; and direct shear where fluid access and stress conditions can be complex). In this paper we combine measurements of shear strength, frictional stability, and permeability for both sheared and unsheared clay-rich

gouges under a wide range of effective normal stresses, shear strains, and sliding velocities. We obtain friction and permeability data simultaneously from *in situ* measurements and explore coupled evolution of permeability and frictional behavior as a function of shear strain.

2. Experimental Methods

[6] We test three clay-rich fault gouges, each containing a significant proportion of a different major clay mineral. Naturally occurring chlorite schist and illite shale are used as chlorite-rich and illite-rich gouges, respectively. Our montmorillonite-rich gouge is a synthetic 50–50 wt% mixture of commercially obtained Ca-montmorillonite (Ca-MM) and silt-sized quartz. The chlorite schist and illite shale were powdered in a disk mill and sieved to $<106 \mu\text{m}$ grain size. For the illite shale, X-ray diffraction (XRD) analysis shows that the bulk powder is primarily composed of illite (59%), quartz (23%), kaolinite/dickite (9%), and plagioclase (4%), with the modal percentages of individual clay minerals determined by XRD analysis of clay separates [Saffer and Marone, 2003]. The chlorite schist is composed of chlorite (46%), plagioclase (35%), quartz (12%), and illite (6%). Mean grain size of the Ca-MM is $60 \mu\text{m}$ with 80% of the grain diameters between 3 and $142 \mu\text{m}$, determined by laser obscuration in a Malvern Mastersizer [e.g., Ikari et al., 2007]. Scanning electron microscope (SEM) images of the materials we studied indicate that the montmorillonite/quartz mixture and illite shale have a similar grain size and grain size distribution, whereas the chlorite schist has a larger average grain size and a smaller proportion of small grains (Figures 1a–1c). Based on the SEM imaging, the large fragments in the chlorite gouge appear to be aggregates of smaller clay grains (Figures 1d–1f). Kaolinite gouge is not included in this study, but an extensive study of the strength and permeability of kaolinite-rich gouge was performed by Crawford et al. [2008].

[7] A total of 15 experiments were conducted using a pressure vessel within a servocontrolled biaxial testing apparatus under true-triaxial conditions (Figure 2 [Samuelson et al., 2006, 2007]). The pressure vessel is designed to accept a three-block double-direct shear assembly, which is sealed with rubber jackets and subjected to confining pressure (P_c). Two layers of sample fault gouge are sheared between roughened, steel forcing blocks. Sample gouge layers are constructed in a leveling jig to a uniform initial thickness of 4 mm (for 12–25 MPa effective normal stress) or 5 mm (for 42–59 MPa effective normal stress), which compacts to ~ 1.5 – 2.5 mm after shear under applied normal stress. Sample contact area is 30.78 cm^2 (for 12–25 MPa effective normal stress) or 32.94 cm^2 (for 42–59 MPa effective normal stress).

[8] Normal stress on the gouge layer is applied by a combination of the confining pressure P_c and a piston that enters the vessel through a dynamic seal (Figures 2b–2c). The applied load and P_c are independently controlled via a fast-acting hydraulic servo mechanism. The gouge layers are sheared by driving the center block with a vertical piston and hydraulic ram. Normal and shear loads are measured to a precision of $\pm 0.1 \text{ kN}$. Confining fluid is food-grade heat transfer oil (XCELTERM 600, Radco Industries) and pore fluid is deionized water in order to minimize the effects of

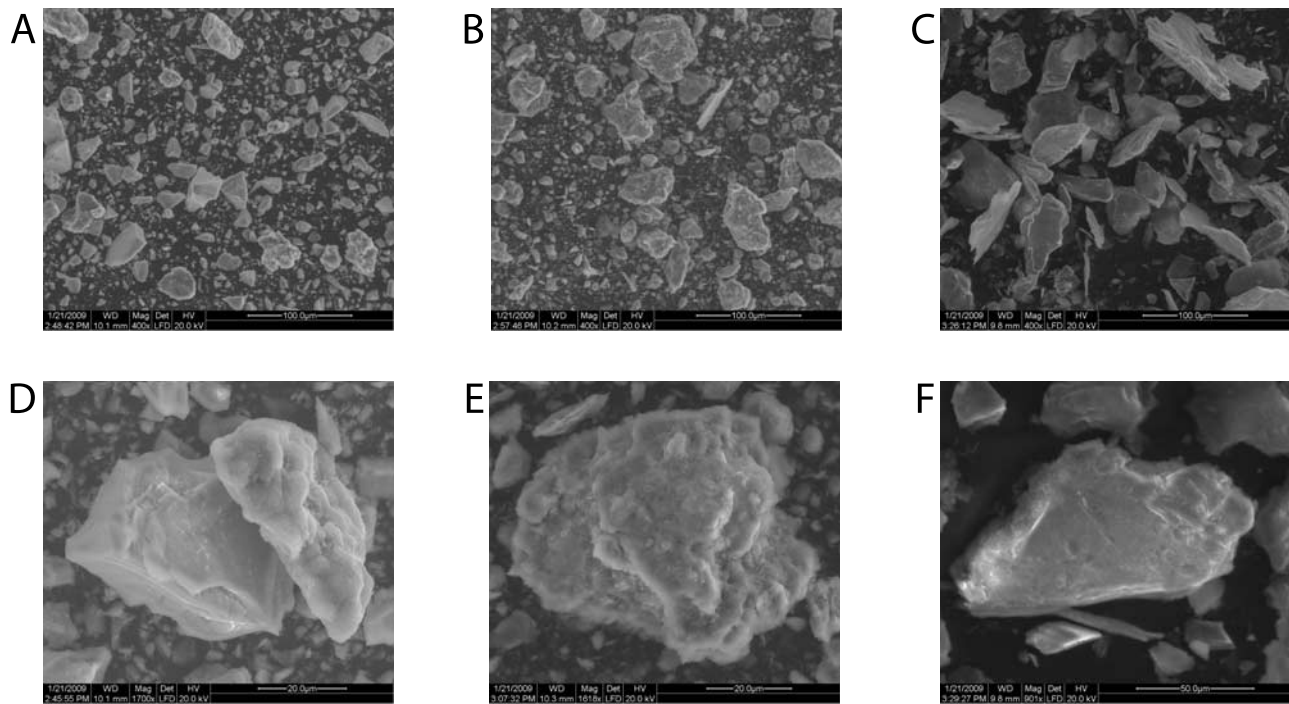


Figure 1. SEM images of the bulk starting material used as gouge at 400 \times magnification: (a) montmorillonite/quartz, (b) illite shale, (c) chlorite schist. (d) Close-up view of an individual (left) quartz grain and (right) montmorillonite aggregate. (e and f) Aggregates of illite and chlorite, respectively.

water chemistry changes due to buffering from interaction with the gouge [e.g., Faulkner and Rutter, 2000]. Effective normal stress is held constant and shear is imposed by controlling the vertical load point displacement external to the pressure vessel. Displacement at both the vertical and horizontal load points is measured to a precision of $\pm 0.02 \mu\text{m}$. True shear displacement and sliding velocity at the layer boundaries are calculated after accounting for apparatus stiffness [see Ikari et al., 2007] and compression of the rubber jackets. The effect of seal friction on the pistons that enter the pressure vessel contributes less than 1.5% of the measured shear stress values.

[9] Pore fluid access is via NPT fittings in the pressure vessel and forcing blocks, and flexible tubing allows displacement parallel and normal to the gouge layers (Figure 2). The inner diameter of the tubing is 1.75 mm. Each forcing block has internal conduits and distribution channels that supply pore fluid to sintered stainless steel frits in contact with the layers, which provide even distribution of fluid over the entire area of the layer. Filter paper between the sample and the frits on the downstream end prevents the frit permeability from being reduced by clogging with fine particles. The system is capable of maintaining two independent pore pressures. We refer to the fluid pressure of the center block and the center block side of each layer as P_{p_a} , and the side blocks as P_{p_b} . For the experiments described in this paper, fluid flow is directed normal to the layers and to the shear direction. Each of the three pressures, P_c , P_{p_a} , and P_{p_b} are independently servocontrolled and can operate in pressure or flow (displacement) control. All three pressures are measured or controlled to $\pm 7 \text{ kPa}$, and fluid volume is measured or controlled to $\pm 1.6 \times 10^{-10} \text{ m}^3$. In the case of the pore pressure, displacement control is used to apply

either a constant flow rate or closed boundary condition, and pressure control is used to apply a constant pressure boundary condition.

[10] Each of our experiments consists of three stages, which yield both frictional and hydrologic data. Initially, we

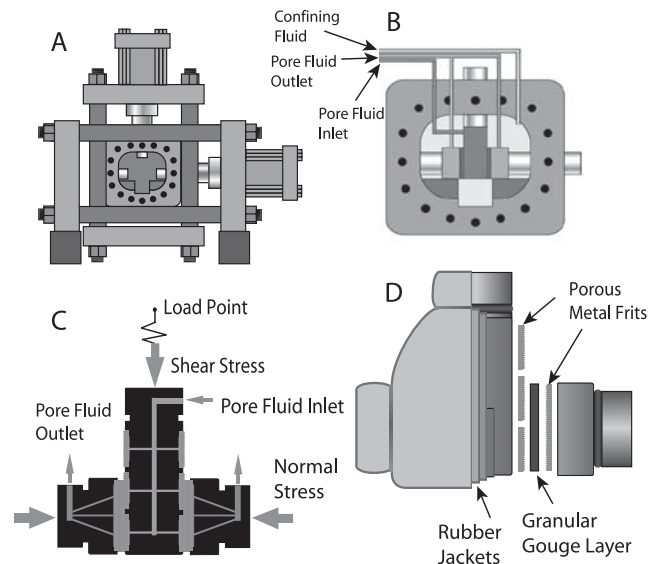


Figure 2. (a) Biaxial stressing apparatus with pressure vessel. (b) Three-block assembly inside pressure vessel showing fluid lines. (c) Internal plumbing structure of three-block sample assembly showing pore fluid inlet and outlets. (d) Three-block sample assembly showing sample gouge layer, porous metal frits, and rubber jackets.

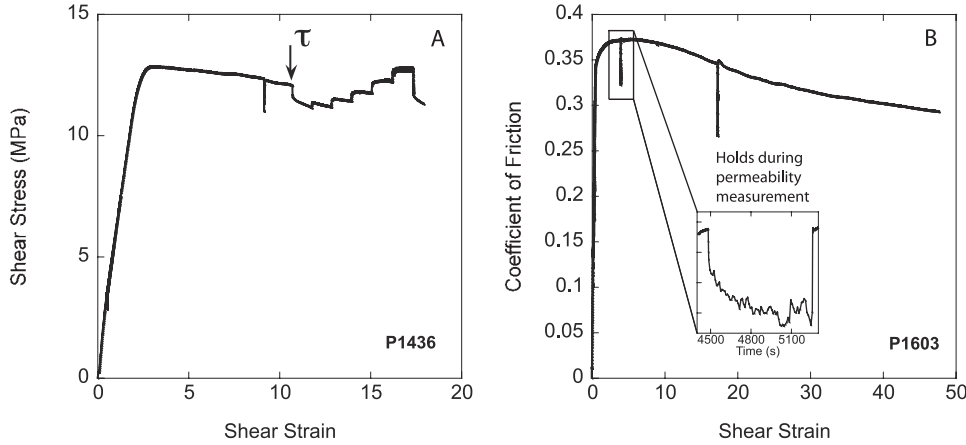


Figure 3. (a) Example of a typical friction experiment. τ indicates displacement at which the residual shear strength value is taken; this value is also used to calculate the coefficient of friction μ . (b) Example of a typical experiment measuring permeability as a function of shear strain. (inset) During a permeability measurement, shearing is stopped and friction relaxes.

saturated all samples at low normal stress (<15 MPa hydrostatic pressure) prior to applying the target effective normal stress to ensure that the layers were uniformly saturated. Stage 1 consists of measuring the layer-perpendicular permeability prior to shearing by applying a constant fluid pressure gradient (0.5–6 MPa) across the sample and conducting a steady state flow-through test. Stage 2 consists of shearing at a constant pore pressure of 5 MPa (Figure 3a). During shear, a velocity-stepping test is conducted to measure frictional constitutive properties. In Stage 3, after termination of shearing, a pore pressure gradient is again imposed in order to measure postshear permeability in the same manner as Stage 1. Shear stress is not removed during the permeability measurement, but relaxes to a residual value under a condition of zero shear displacement rate, in a similar manner to that observed in conventional slide-hold-slide friction tests (inset, Figure 3b). In addition, we conducted trial experiments in which the fluid pressure gradient was applied during shear. These dynamic permeability measurements yield very similar results to those we obtained during Stage 3; however for consistency between

experiments and to minimize the effect of shear during the flow measurements, we report only permeability values under the quasistatic conditions (as in Stages 1 and 3).

[11] We also conducted three experiments in which permeability was measured as a function of shear displacement (Figure 3b). These experiments were conducted once for each gouge composition at an effective stress of 32 MPa. In these experiments, shearing was paused and permeability was measured at load point displacements of ~3, 5, 7, and 12 mm in addition to the preshear and postshear measurements using the same flow-through technique described above. Similar to the postshear permeability measurements described above (Stage 2), shear stress relaxes via creep during the permeability measurements. Table 1 lists the experimental parameters for all experiments in this study.

2.1. Friction Measurements

[12] During shear (Stage 2), pore pressure at the upstream end of the sample (P_{p_a}) was held constant at 5 MPa, while at the downstream end (controlled by P_{p_b}) a no-flow condition was imposed in order to document any overpressure gener-

Table 1. Experiment Parameters

Experiment	Gouge	σ'_n (MPa)	P_c (MPa)	P_p (MPa) ^a	Sliding Velocity ($\mu\text{m/s}$)	Layer Thickness Under Load (μm)	Maximum Shear Strain
p1421	montmorillonite/quartz	12	6	5	1, 3, 10, 30, 100, 300	2085	8.9
p1418	montmorillonite/quartz	25	12	5	1, 3, 10, 30, 100, 300	2115	8.9
p1500	montmorillonite/quartz	43	20	5	0.5, 1.6, 5.3, 16, 53, 158	2065	5.2
p1535	montmorillonite/quartz	58	28	5	0.5, 1.6, 5.3, 16, 53, 158	2785	4.0
p1427	illite shale	12	6	5	1, 3, 10, 30, 100, 300	1310	10.3
p1426	illite shale	25	12	5	1, 3, 10, 30, 100, 300	1620	11.2
p1437	illite shale	42	20	5	1, 3, 10, 30, 100, 300	1510	16.5
p1521	illite shale	58	28	5	0.5, 1.6, 5.3, 16, 53, 158	1515	8.3
p1423	chlorite schist	12	6	5	1, 3, 10, 30, 100, 300	905	22.8
p1422	chlorite schist	25	12	5	1, 3, 10, 30, 100, 300	1540	13.4
p1436	chlorite schist	42	20	5	1, 3, 10, 30, 100, 300	1340	17.9
p1534	chlorite schist	59	28	5	0.5, 1.6, 5.3, 16, 53, 158	1730	6.5
p1608	montmorillonite/quartz	32	12	5	11	1755	21.2
p1602	illite shale	32	12	5	11	1685	25.6
p1603	chlorite schist	32	12	5	11	1180	47.8

^aPore pressure during shear, controlled by P_{p_a} .

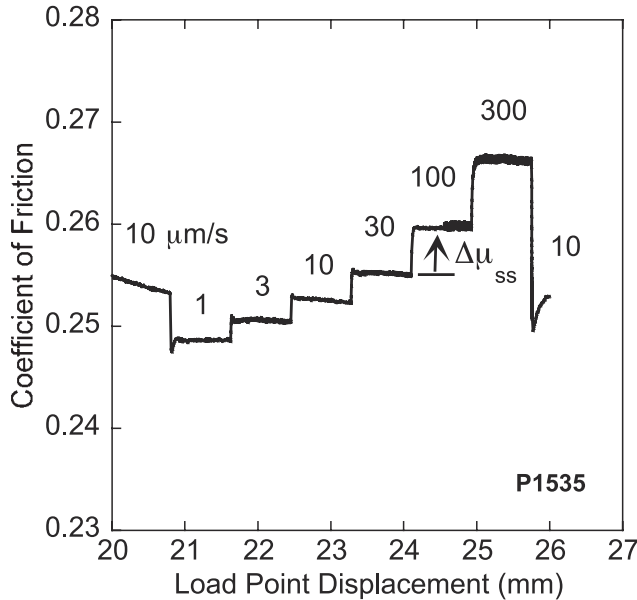


Figure 4. Example of a velocity-stepping test. Load point velocity is increased in discrete steps; resulting measured change in steady state friction is used to calculate the rate and state parameters a , b , $a - b$, and D_c . Constant, long-term friction trends are removed.

ated during shear and evaluate our control of P_p in the layer. The samples were sheared at a constant velocity of 5 or 11 $\mu\text{m/s}$ until steady state shear strength was achieved (Figure 3a). The velocity was then increased stepwise from 0.5–300 $\mu\text{m/s}$ in velocity-stepping tests (Figure 4 [e.g., Marone, 1998]). Shear displacement during each velocity step was 400 or 800 μm . Maximum shear displacement for these layers was 36 mm; shearing was typically terminated at displacements of ~ 20 mm. Due to differences in initial layer thickness and total displacement, maximum shear strain ranged between 4 and 48. In some experiments, we observed a slight increase in pore pressure (as measured in P_{p_b}) as a result of shearing in the low permeability samples. These pore pressure transients represent a maximum of 3% of the total effective stress, and are typically $\ll 1\%$.

[13] The steady state shear stress τ was measured prior to the initiation of the velocity-stepping test. The coefficient of sliding friction μ was then calculated as

$$\tau = \mu \sigma'_n + c, \quad (1)$$

[Handin, 1969; Byerlee, 1978] where c is cohesion, and the effective normal stress σ'_n is the difference between the applied normal stress σ_n and the pore fluid pressure:

$$\sigma'_n = \sigma_n - P_p. \quad (2)$$

The pore pressure P_p is taken as the average of the pore pressure at the drained and undrained boundaries. Maximum error in effective normal stress due to the differing boundary conditions described above is $< 1.3\%$. The cohesion c is assumed to be negligible for the unconsolidated gouge used in our experiments.

[14] We quantify frictional stability using the friction rate parameter $a - b$; defined as

$$a - b = \frac{\Delta \mu_{ss}}{\ln(V/V_o)}, \quad (3)$$

where $\Delta \mu_{ss}$ is the change in the steady state coefficient of friction upon an instantaneous change in sliding velocity from V_o to V [e.g., Marone, 1998]. Positive $a - b$ values indicate velocity-strengthening behavior, whereas negative $a - b$ values indicate velocity-weakening behavior. Velocity weakening is a prerequisite for stick-slip behavior which is associated with earthquake nucleation [Dieterich and Kilgore, 1996; Marone, 1998; Scholz, 2002]. Equation (3) represents the steady state form of Dieterich's [1979, 1981] constitutive law describing rate-dependent and state-dependent frictional behavior:

$$\mu = \mu_o + a \ln\left(\frac{V}{V_o}\right) + b \ln\left(\frac{V_o \Theta}{D_c}\right), \quad (4)$$

$$\frac{d\Theta}{dt} = 1 - \frac{V_o \Theta}{D_c}, \quad (5)$$

where a and b are empirically derived constants (unitless), Θ is the state variable (units of time), and D_c is the critical slip distance. The state variable is inferred to be the average lifetime of contact points that control friction, and the critical slip distance is the displacement over which those contacts are renewed. Under steady state sliding conditions, the average time that a contact exists is constant, reducing the left side of equation (5) to zero, and substitution of the state variable at steady state Θ_{ss} into equation (4) yields equation (3).

[15] To obtain the values of the constitutive parameters a , b , and D_c , we model the velocity step data following Saffer and Marone [2003]. The interaction of the sample with its elastic surroundings is incorporated according to the equation:

$$\frac{d\mu}{dt} = K(V_{lp} - V), \quad (6)$$

where K is the stiffness of the fault surroundings (in this case the testing apparatus and sample blocks) normalized by normal stress ($K = \sim 3 \times 10^{-3} \mu\text{m}^{-1}$ at 25 MPa normal stress), V_{lp} is the load point velocity, and V is the true slip velocity. We then solve equations (5) and (6) simultaneously, with equation (4) as a constraint, using a fifth-order Runge-Kutta method. The constitutive parameters are then obtained as solutions to a nonlinear inverse problem using an iterative least squares method (Figure 5 [Reinen and Weeks, 1993; Blanpied et al., 1998; Saffer and Marone, 2003]).

[16] The pore pressure in equation (2) used to calculate the shear stress is an average of the pore pressure at the drained (P_{p_a}) and undrained (P_{p_b}) ends of the sample. The measurement of pore pressure at the undrained sample boundary also provides a method for quantifying the potential effects of pore pressure transients on our reported

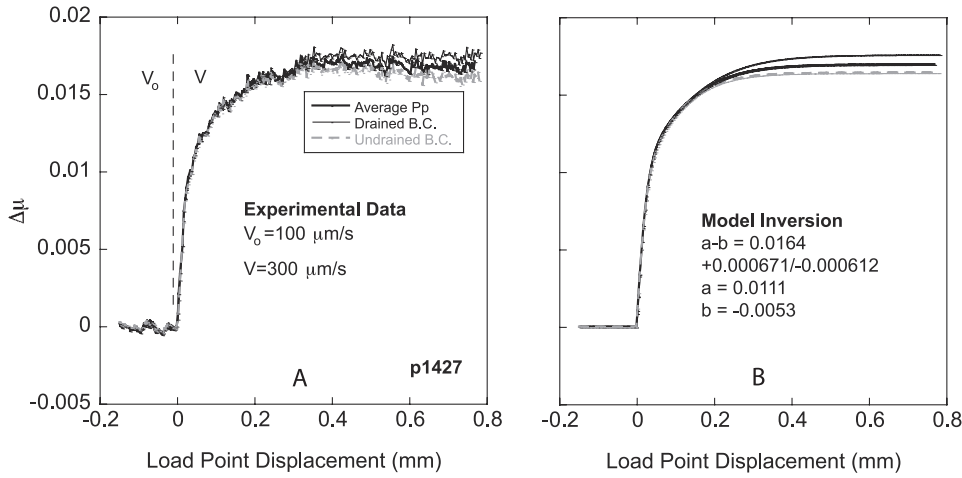


Figure 5. (a) Example of experimental data from an individual velocity step. (b) Model inversion of the velocity step in Figure 5a. Three curves are shown for both the experimental data and model, with friction calculated using average pore pressure, pore pressure at the (controlled P_p) drained boundary, and pore pressure measured at the undrained boundary. Differences between the curves represent the maximum variation due to different boundary conditions.

values of frictional strength (μ) and constitutive parameters ($a - b$, a , and b). To quantify the uncertainty associated with this effect, we report upper and lower bounds on all frictional properties, computed using the pore pressure at the drained boundary and at the undrained boundary of the layer as minima and maxima on P_p in equation (2). The error is extremely small; data and model inversions for friction calculated using average pore pressure (reported in the results section and Table 2), pore pressure at the undrained boundary, and pore pressure at the drained boundary are all within 3.5% (Figure 5). The example shown in Figure 5 is from the velocity step that had largest variation between pore pressure boundary conditions in any of our experiments. This indicates that our constitutive modeling results are insensitive to transient pore pressure effects caused by differing sample boundary conditions, unless rapid changes in pore pressure within the gouge layer are not accurately tracked by the measurement of P_{p_b} due to the finite volume and compliance of the “downstream” fluid reservoir that causes a damping and delay of the signal at the measurement point. We discuss this possibility in detail below (section 4.2.2).

2.2. Permeability Measurements

[17] In each individual flow-through permeability test (Stages 1 and 3), we imposed a constant fluid pressure normal to the layer, and calculated permeability from the resulting flow rate across the sample after reaching steady state (Figure 6) according to Darcy’s law:

$$Q = \frac{kA}{\eta} \frac{dP_p}{dx}, \quad (7)$$

where Q is the volumetric flow rate ($\text{m}^3 \text{s}^{-1}$), k is the sample permeability (m^2), A is the cross-sectional area of the sample (m^2), η is the viscosity of water (Pa s), dP_p is the imposed fluid pressure difference across the sample, and

dx is the layer thickness. We calculate permeability, k , using $\eta = 1.12 \times 10^{-3} \text{ Pa s}$ and $A = 0.005 \text{ m}^2$ (this is the area of the permeable frit, which is slightly smaller than the area of the forcing blocks). Two volumetric flow rates are measured, one from the sample inlet (P_{p_a}) and one from the sample outlet (P_{p_b}) (Figure 6). We define Q as the average flow rate and consider the system to be at steady state only when $Q_a = Q_b$ to within <5%.

3. Results

3.1. Frictional Strength

[18] We measured overall shear strength of the fault gouge (τ) and coefficient of sliding friction (μ) after attaining a residual, or steady state, shear strength (Figure 3). The stress-strain curves typically exhibit a peak shear stress and rollover to a residual value at shear strains of ≤ 5 . Montmorillonite gouges show a prominent stress peak and decay, whereas chlorite and illite gouges show a gradual rollover without a strong peak. All gouge strength and coefficient of friction values are low (Figure 7), with $\mu < 0.35$. Chlorite and illite gouge are nearly identical in strength, with μ ranging from 0.27 to 0.32. However, montmorillonite gouge is significantly weaker than illite and chlorite gouge, with $\mu = 0.19$ –0.23. There is no clear dependence of μ on effective normal stress (Figure 7).

3.2. Frictional Constitutive Properties

[19] All three of the gouges exhibit velocity-strengthening frictional behavior (Figure 8; Table 2). Values of $a - b$ for illite gouge range from ~ 0.003 to 0.010 ; $a - b$ ranges from ~ 0.001 to 0.006 for montmorillonite gouge and ~ 0.003 to 0.010 for chlorite gouge (Figure 8). We find that $a - b$ is independent of effective normal stress in all cases, but exhibits a positive dependence on sliding velocity with values increasing by ~ 0.002 per order of magnitude increase in upstep velocity for all three gouges (Figures 8–9). In all cases, we find that $a > b$ (Figures 10–11; Table 2).

Table 2. Constitutive Parameters for Least Squares Fit of the Dieterich Law

Experiment	Gouge	σ'_n (MPa)	V_o ($\mu\text{m/s}$)	V ($\mu\text{m/s}$)	a	b	$a - b$	D_c (μm)	a SD	b SD	D_c SD
p1421	montmorillonite/quartz	12	1	3	0.0012	0.0003	0.0009	14.2	0.00005	0.00005	4.13
p1418	montmorillonite/quartz	25	1	3	0.0019	0.0003	0.0017	10.8	0.00004	0.00004	2.03
p1500	montmorillonite/quartz	43	0.5	1.6	0.0015	0.0008	0.0007	5.9	0.00003	0.00003	0.25
p1535	montmorillonite/quartz	58	0.5	1.6	0.0018	0.0005	0.0012	8.2	0.00002	0.00002	0.32
p1421	montmorillonite/quartz	12	3	10	0.0016	-0.0001	0.0017	25.9	0.00005	0.00005	25.82
p1418	montmorillonite/quartz	25	3	10	0.0022	-0.0002	0.0024	117.2	0.00002	0.00002	27.40
p1500	montmorillonite/quartz	43	1.6	5.3	0.0018	0.0009	0.0009	5.4	0.00004	0.00004	0.30
p1535	montmorillonite/quartz	58	1.6	5.3	0.0023	0.0005	0.0018	4.7	0.00004	0.00004	0.48
p1421	montmorillonite/quartz	12	10	30	0.0022	-0.0009	0.0031	78.3	0.00008	0.00006	9.17
p1418	montmorillonite/quartz	25	10	30	0.0031	-0.0004	0.0035	87.3	0.00006	0.00005	28.14
p1500	montmorillonite/quartz	43	5.3	16	0.0022	0.0007	0.0014	10.0	0.00002	0.00002	0.34
p1535	montmorillonite/quartz	58	5.3	16	0.0025	0.0002	0.0023	7.0	0.00004	0.00003	1.28
p1421	montmorillonite/quartz	12	30	100	0.0037	-0.0012	0.0049	88.6	0.00022	0.00020	23.86
p1418	montmorillonite/quartz	25	30	100	0.0039	-0.0004	0.0042	38.4	0.00011	0.00010	24.95
p1500	montmorillonite/quartz	43	16	53	0.0032	0.0006	0.0025	19.6	0.00004	0.00003	1.56
p1535	montmorillonite/quartz	58	16	53	0.0034	0.0001	0.0033	30.0	0.00002	0.00002	10.27
p1421	montmorillonite/quartz	12	100	300	0.0059	-0.0032	0.0091	102.6	0.00020	0.00018	10.14
p1418	montmorillonite/quartz	25	100	300	0.0069	-0.0003	0.0072	78.5	0.00018	0.00017	104.76
p1500	montmorillonite/quartz	43	53	158	0.0048	-0.0004	0.0052	33.3	0.00002	0.00002	3.10
p1535	montmorillonite/quartz	58	53	158	0.0051	-0.0002	0.0053	37.0	0.00003	0.00002	7.08
p1427	illite shale	12	1	3	0.0041	0.0002	0.0039	52.8	0.00004	0.00004	47.05
p1426	illite shale	25	1	3	0.0052	0.0008	0.0044	14.8	0.00006	0.00005	1.21
p1437	illite shale	42	1	3	0.0046	0.0013	0.0034	44.4	0.00002	0.00002	0.89
p1521	illite shale	58	0.5	1.6	0.0040	0.0014	0.0026	45.1	0.00004	0.00003	1.53
p1427	illite shale	12	3	10	0.0048	-0.0003	0.0051	79.4	0.00004	0.00004	34.05
p1426	illite shale	25	3	10	0.0053	0.0017	0.0036	92.3	0.00003	0.00002	2.22
p1437	illite shale	42	3	10	0.0057	0.0022	0.0035	99.9	0.00002	0.00002	1.35
p1521	illite shale	58	1.6	5.3	0.0051	0.0010	0.0041	52.2	0.00003	0.00003	3.16
p1427	illite shale	12	10	30	0.0059	0.0009	0.0050	2297.1	0.00007	0.00024	702.78
p1426	illite shale	25	10	30	0.0062	-0.0005	0.0066	91.9	0.00005	0.00004	11.20
p1437	illite shale	42	10	30	0.0163	0.0098	0.0066	1.5	0.00001	0.00001	0.07
p1521	illite shale	58	5.3	16	0.0054	-0.0004	0.0058	346.3	0.00001	0.00007	85.44
p1427	illite shale	12	30	100	0.0062	-0.0029	0.0091	17.7	0.00087	0.00086	7.71
p1426	illite shale	25	30	100	0.0069	-0.0001	0.0070	23.6	0.00003	0.00024	192.74
p1437	illite shale	42	30	100	0.0072	-0.0019	0.0091	105.5	0.00005	0.00004	3.92
p1521	illite shale	58	16	53	0.0059	-0.0006	0.0065	32.1	0.00003	0.00002	2.10
p1427	illite shale	12	100	300	0.0095	-0.0066	0.0161	84.9	0.00035	0.00032	6.57
p1426	illite shale	25	100	300	0.0078	-0.0007	0.0085	539.5	0.00011	0.00244	48736.14
p1437	illite shale	42	100	300	0.0075	-0.0013	0.0088	1053.4	0.00007	0.00331	20520.65
p1421	illite shale	58	53	158	0.0057	-0.0016	0.0073	33.2	0.00004	0.00004	1.16
p1423	chlorite schist	12	1	3	0.0062	-0.0076	0.0138	123.4	0.00006	0.00004	1.66
p1422	chlorite schist	25	1	3	0.0040	-0.0022	0.0062	53.6	0.00003	0.00002	0.87
p1436	chlorite schist	42	1	3	0.0042	-0.0003	0.0045	30.5	0.00003	0.00002	2.93
p1534	chlorite schist	59	0.5	1.6	0.0035	-0.0006	0.0029	8.9	0.00003	0.00003	0.49
p1423	chlorite schist	12	3	10	0.0077	-0.0122	0.0198	182.4	0.00007	0.00007	2.73
p1422	chlorite schist	25	3	10	0.0046	-0.0010	0.0055	37.7	0.00008	0.00008	4.65
p1436	chlorite schist	42	3	10	0.0056	-0.0014	0.0069	43.9	0.00003	0.00003	1.38
p1534	chlorite schist	59	1.6	5.3	0.0041	-0.0005	0.0035	5.8	0.00010	0.00010	1.42
p1423	chlorite schist	12	10	30	0.0047	-0.0014	0.0062	9.0	0.00026	0.00025	2.15
p1422	chlorite schist	25	10	30	0.0055	-0.0013	0.0067	31.1	0.00008	0.00007	2.34
p1436	chlorite schist	42	10	30	0.0069	-0.0021	0.0091	106.3	0.00002	0.00002	1.66
p1434	chlorite schist	59	5.3	16	0.0061	-0.0014	0.0047	1.6	0.00027	0.00027	0.34
p1423	chlorite schist	12	30	100	0.0076	-0.0015	0.0091	29.9	0.00020	0.00019	5.40
p1422	chlorite schist	25	30	100	0.0063	-0.0017	0.0080	46.2	0.00015	0.00015	5.51
p1436	chlorite schist	42	30	100	0.0071	-0.0012	0.0083	34.6	0.00007	0.00007	2.76
p1434	chlorite schist	59	16	53	0.0057	-0.0007	0.0050	11.0	0.00006	0.00005	1.06
p1423	chlorite schist	12	100	300	0.0107	-0.0040	0.0147	56.0	0.00036	0.00034	7.15
p1422	chlorite schist	25	100	300	0.0087	-0.0016	0.0103	57.8	0.00019	0.00018	10.28
p1436	chlorite schist	42	100	300	0.0076	-0.0026	0.0103	67.8	0.00015	0.00014	5.51
p1534	chlorite schist	59	53	158	0.0069	0.0002	0.0067	3.1	0.00033	0.00033	9.67

Values of a cluster between 0.010 and 0.001 and are generally insensitive to effective normal stress. Values of a for montmorillonite gouge are generally lower (most are <0.005) than those for illite and chlorite gouges. As is the case for $(a - b)$, values of a for all three gouge types exhibit a positive dependence on sliding velocity (Figure 11). In contrast, values of b exhibit varying amounts of scatter for each gouge type, and most values cluster near 0 (Figure 10).

These values are generally independent of normal stress and sliding velocity, but with some exceptions the most negative values of b are associated with low effective normal stress and high sliding velocity. The velocity dependence of $a - b$ results from positive rate dependence of a and a negative or neutral rate dependence of b (Figures 9–11). The critical slip distance D_c exhibits substantial scatter but is generally on the order of tens of microns, and is insensitive to both

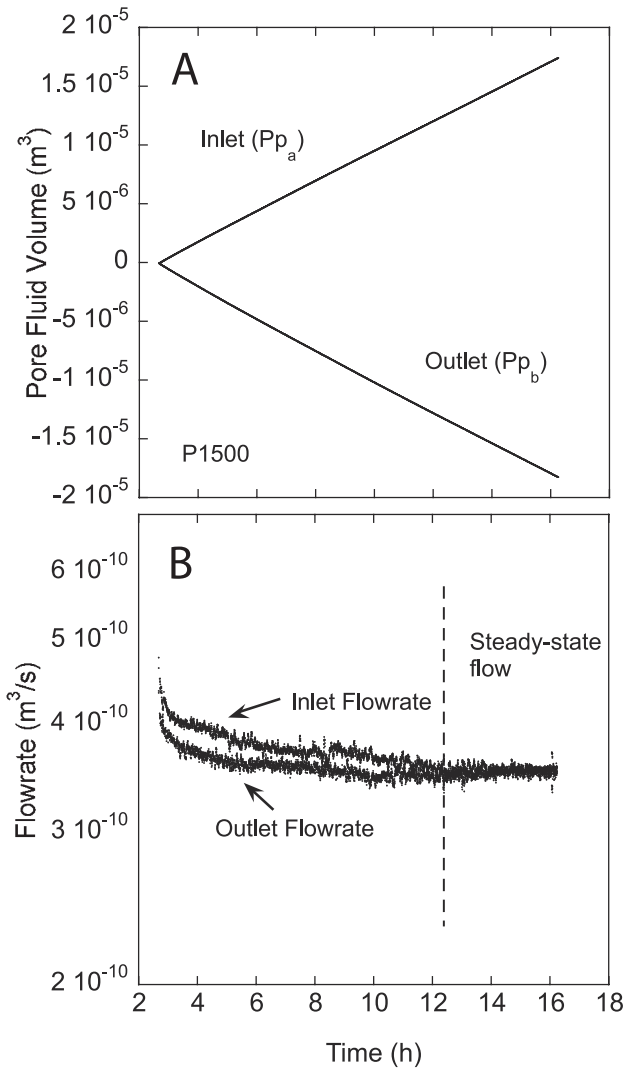


Figure 6. Example of a typical permeability experiment. (a) Displacement of pore fluid (inlet) into and (outlet) out of sample layer versus time. (b) Volumetric flow rate of fluid into and out of sample layer with time. Permeability is measured when steady state flow is achieved.

effective normal stress and sliding velocity (Table 2). It should be noted that for values of b approaching 0, D_c is undefined and thus uncertainty is large.

3.3. Dilation

[20] We measured dilation of the gouge layer in response to step increases in sliding velocity, and report it using the parameter α :

$$\alpha = \frac{\Delta h}{\ln\left(\frac{V}{V_o}\right)}, \quad (8)$$

where Δh is the change in layer thickness in response to a velocity change from V to V_o [Marone and Kilgore, 1993]. Dilatancy of fault gouge has important implications for the evolution of macroscopic fault frictional properties because

(1) it may cause strengthening by depressurization of pore fluid [Segall and Rice, 1995; Samuelson et al., 2007], (2) it tends to counteract thermal pressurization, and (3) it may enhance shear localization [Marone and Kilgore, 1993]. Furthermore, changes in dilatancy rate have been linked to velocity-strengthening behavior [Marone et al., 1990]. We observe consistently positive values of α for all experimental conditions in this study (0.2–1.9 μm , Figure 12). No discernible trend in α is observed with sliding velocity.

3.4. Permeability

[21] The chlorite gouge exhibits the highest permeability over the entire range of effective normal stresses, both before and after shearing, with permeability ranging from $1.4 \times 10^{-17} \text{ m}^2$ to $3.6 \times 10^{-16} \text{ m}^2$ before shear, and $7.9 \times 10^{-19} \text{ m}^2$ to $6.0 \times 10^{-17} \text{ m}^2$ after shear (shear strains of 7–23). Montmorillonite and illite gouge permeabilities are lower than that of chlorite, however before shearing mont-

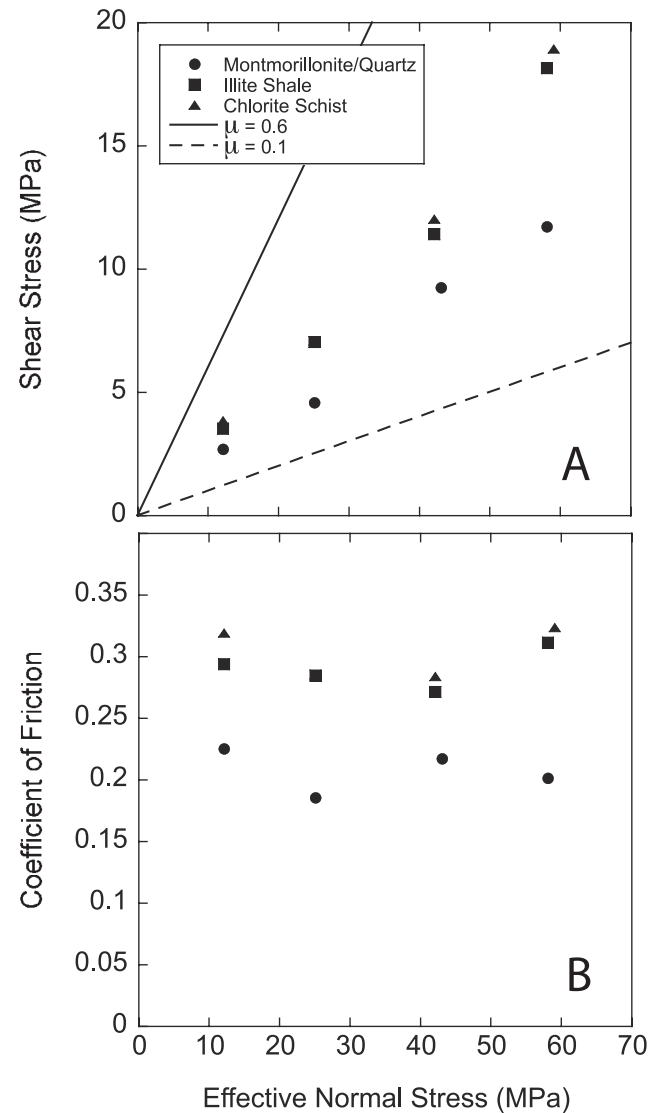


Figure 7. (a) Residual shear stress versus effective normal stress in a Coulomb-Mohr diagram. Friction envelopes for $\mu = 0.6$ and $\mu = 0.1$ are shown for reference. (b) Coefficient of friction versus effective normal stress.

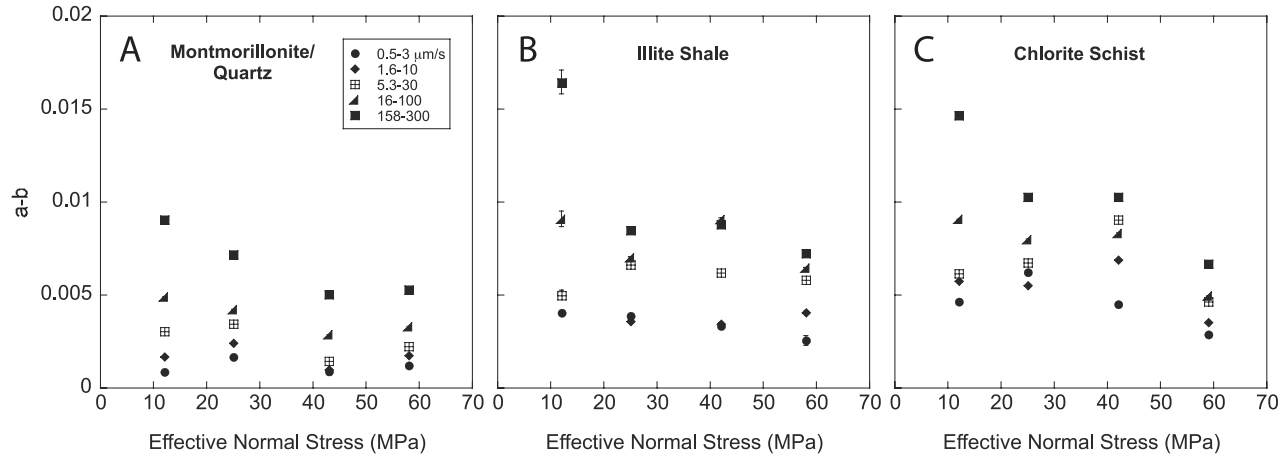


Figure 8. $a - b$ versus effective normal stress for (a) montmorillonite-rich gouge, (b) illite-rich gouge, and (c) chlorite-rich gouge. Uncertainty in individual friction parameters due to small pore pressure transients in the layer as described in the text (see Figure 4) are shown by error bars, which are smaller than the symbols in most cases.

morillonite permeability is similar to that of chlorite and illite permeability is significantly lower. After shear, both montmorillonite and illite gouges are significantly less permeable than the chlorite gouge (Figure 13); the permeability of the montmorillonite gouge ranges from $1.1 \times 10^{-17} \text{ m}^2$ to $2.6 \times 10^{-16} \text{ m}^2$ before shear, and decreases to $1.7 \times 10^{-20} \text{ m}^2$ to $2.5 \times 10^{-19} \text{ m}^2$ after shear. For illite gouge, permeability ranges from $7.5 \times 10^{-20} \text{ m}^2$ to $5.0 \times 10^{-17} \text{ m}^2$ before shear, and decreases to $8.3 \times 10^{-21} \text{ m}^2$ to $4.4 \times 10^{-19} \text{ m}^2$ after shear. For the montmorillonite and chlorite gouges (both before and after shear), increased effective normal stress reduces permeability only up to $\sim 35 \text{ MPa}$, above which k is independent of effective normal stress. In contrast, permeability of illite gouge decreases, with some scatter, over the entire range of effective normal stress.

[22] As expected, preshear permeability is consistently higher than postshear permeability. However, the effect of shear on permeability differs between gouges (Figure 14). Shear induced permeability reduction is greatest early in the

strain history for all three materials, dropping rapidly up to shear strains of ~ 5 before approaching a steady value at higher strains. However, the montmorillonite permeability decreases by a factor of ~ 1000 , whereas the permeability of illite gouge is only reduced by a factor of ~ 10 and chlorite gouge by a factor of ~ 20 .

4. Discussion

4.1. Comparison to Previous Data

[23] Our results are consistent with existing friction and hydrologic data, but are more comprehensive and systematic than previous studies. Our steady state friction values for illite shale and montmorillonite-quartz ($\mu = 0.27\text{--}0.32$ and $\mu = 0.19\text{--}0.23$, respectively) are significantly lower than previously reported values obtained from experiments run under understaturated conditions ($\mu = 0.50\text{--}0.60$ and $\mu = 0.27\text{--}0.50$, respectively [Saffer and Marone, 2003; Ikari et al., 2007]). This is consistent with results from our previous work [Ikari et al., 2007] and with other data [Morrow et al.,

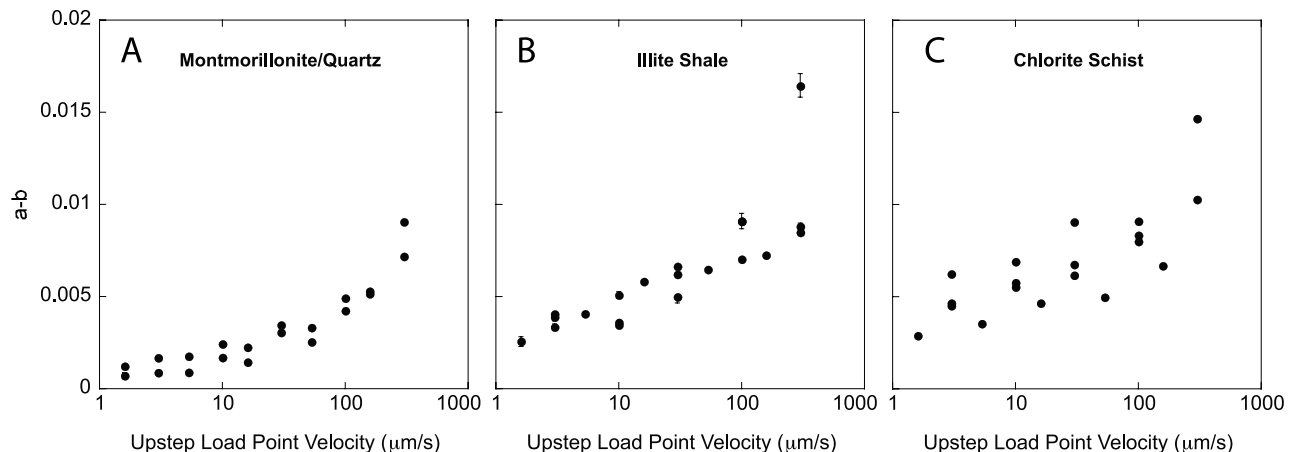


Figure 9. $a - b$ versus upstep load point velocity for (a) montmorillonite-rich gouge, (b) illite-rich gouge, and (c) chlorite-rich gouge. Error bars are determined as described for Figure 8.

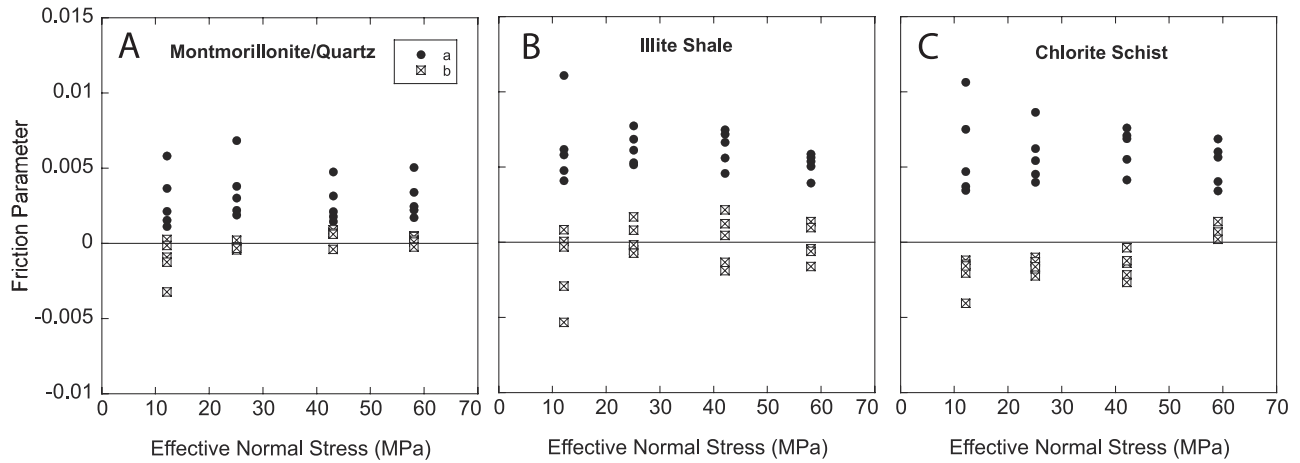


Figure 10. Constitutive parameters a and b versus effective normal stress for (a) montmorillonite-rich gouge, (b) illite-rich gouge, and (c) chlorite-rich gouge. Error bars are determined as described for Figure 7.

2000; *Moore and Lockner*, 2004] showing that water saturation of phyllosilicate minerals reduces frictional strength by as much as 60%.

[24] For chlorite gouge, our observed friction values of $\mu = 0.27\text{--}0.32$ are similar to a reported value of $\mu = \sim 0.38$ for saturated, powdered chlorite schist at 100 MPa effective normal stress [*Moore and Lockner* 2004], especially after accounting for jacketing and apparatus effects that tend to cause strain hardening in the triaxial geometry. *Logan and Rauenzahn* [1987] reported a friction value of ~ 0.30 for a saturated 50–50% montmorillonite-quartz mixture, similar to our upper value of 0.23 for gouge of the same composition. For pure montmorillonite gouge, the values reported by *Morrow et al.* [1992] ($0.18\text{--}0.29$) are significantly higher than values of 0.03–0.16 reported for pure montmorillonite by other authors [*Logan and Rauenzahn*, 1987; *Kopf and Brown*, 2003; *Ikari et al.*, 2007]. Part of this discrepancy is likely related to differences in testing apparatus. *Morrow et al.* [1992] also obtained friction coefficients of ~ 0.38 to 0.48 for a powdered illite shale. The high end of their range is likely due to considerable strain hardening, as noted above, however the lower

end of their range is similar to our results. We note that our friction values for 50–50% montmorillonite-quartz mixtures are comparable to those by *Morrow et al.* [1992] ($0.18\text{--}0.29$) for pure montmorillonite gouge.

[25] *Brown et al.* [2003] and *Kopf and Brown* [2003] report results from seawater-saturated friction experiments performed on both mineral standards and natural clay-rich samples from the Nankai (SW Japan) and Barbados subduction thrusts. Their reported friction values for pure chlorite, illite, and smectite gouges are lower than ours; one likely explanation for this difference is that their gouges were monomineralic, whereas our samples contained ~ 50 wt% quartz [*Logan and Rauenzahn*, 1987; *Saffer and Marone*, 2003; *Ikari et al.*, 2007]. Moreover, the work by *Kopf and Brown* [2003] indicates a negligible dependence of friction on effective normal stress for chlorite and illite, and significantly lower strength of smectite, both of which are highly consistent with our results. *Kopf and Brown* [2003] report friction values in the range of $\mu = 0.10\text{--}0.30$ for natural samples from Nankai and Barbados, and *Brown et al.* [2003] report similarly low friction values ($\mu = 0.17\text{--}0.27$) for samples from Nankai with comparable clay con-

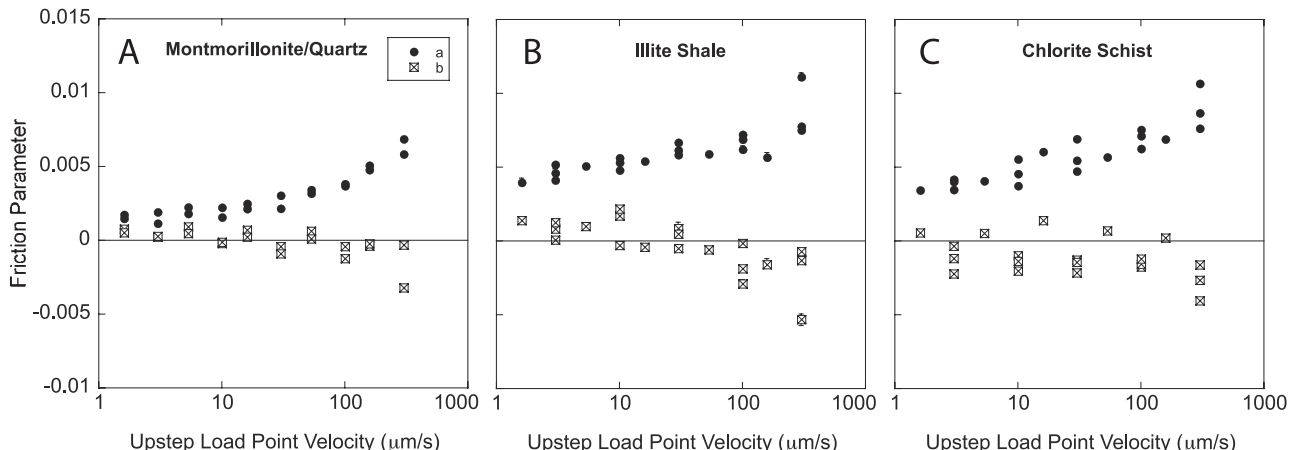


Figure 11. Constitutive parameters a and b versus shear velocity for (a) montmorillonite-rich gouge, (b) illite-rich gouge, and (c) chlorite-rich gouge. Error bars are determined as described for Figure 7.

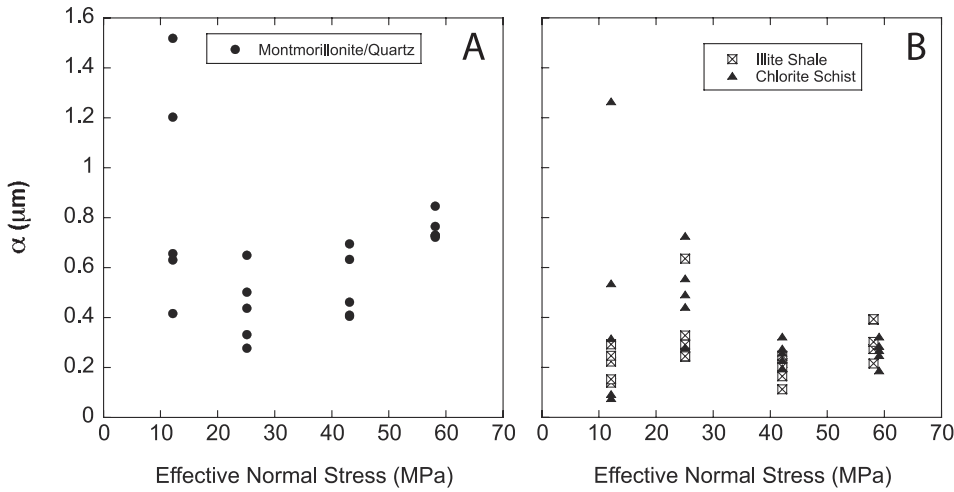


Figure 12. Dilatancy parameter α versus effective normal stress for (a) montmorillonite-rich gouge and (b) illite-rich and chlorite-rich gouge.

tents to our samples. This suggests that our sample gouges can be considered suitable analogs to those from natural fault zones.

[26] Our observation of strong velocity-strengthening behavior for these three gouges also agrees with results from a small number of existing studies of rate-dependent frictional behavior of clay-rich gouges. *Saffer and Marone* [2003] and *Ikari et al.* [2007] found that undersaturated montmorillonite gouges can range from highly velocity strengthening to slightly velocity weakening. *Ikari et al.* [2007] further showed that increased hydration state of montmorillonite tends to inhibit frictional instability, which is consistent with the strong velocity strengthening of the saturated montmorillonite-quartz gouge that we report here. *Logan and Rauenzahn* [1987] also report ($a - b$) values of 0.0010 to 0.0100 for gouges containing 25% to 75% montmorillonite. Although they did not report ($a - b$) values, *Brown et al.* [2003] observed velocity-strengthening behavior in their smectite, illite, and chlorite gouges. *Morrow et al.* [1992] and *Saffer and Marone* [2003] both report consistent velocity strengthening for illite shale. *Morrow et al.* report an ($a - b$) of ~ 0.0050 for a velocity increase from 0.01 to 1 $\mu\text{m/s}$, which is comparable to our observed values for a 1 to 3 $\mu\text{m/s}$ velocity step. *Saffer and Marone* [2003] report ($a - b$) values of ~ 0.0010 to 0.0040, lower than our reported values (0.0037 to 0.0096); however, the gouges in this study were saturated while those in *Saffer and Marone* [2003] were not.

[27] It is likely that the higher $a - b$ values in this study are the result of fully saturated clays and combined clay-granular behavior. However, it is also possible that transient pore pressure reduction due to gouge dilation may contribute to velocity strengthening, based on our consistent observation of dilation with velocity step increases. Dilation values of 0.2–1.9 μm are consistent with previous measurements of dilation in granular fault gouge at shear strains $\gtrsim 5$ [Marone and Kilgore, 1993]. Although we cannot rule out transient reductions in pore pressure within the layers locally at the microscale, we believe these effects are small

because of our data demonstrating negligible changes in the (undrained) downstream pore pressure P_{p_b} (e.g., Figure 5).

[28] Our permeability measurements are also compatible with previous measurements for clay-rich sediments and sheared gouges. For a 50–50% montmorillonite-quartz mixture, *Takahashi et al.* [2007] report a preshear permeability of $2.9 \times 10^{-19} \text{ m}^2$, and postshear permeability of $2.7 \times 10^{-21} \text{ m}^2$ at an effective normal stress of 75 MPa and a shear strain of ~ 3 . At a slightly lower effective normal stress of 58 MPa, we observe very similar values of $9.3 \times 10^{-18} \text{ m}^2$ preshear, and $1.7 \times 10^{-20} \text{ m}^2$ at a shear strain of 4.0. *Faulkner and Rutter* [2003] reported permeabilities for intact gouge from the Carboneras fault, which contained illite and chlorite, but no smectite. At room

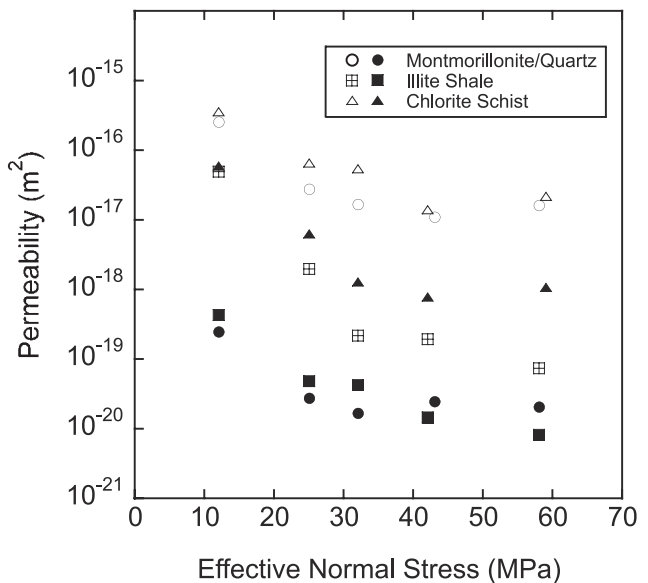


Figure 13. Permeability versus effective normal stress for all three clay gouges. Open symbols indicate preshear permeability; solid symbols indicate post-shear permeability.

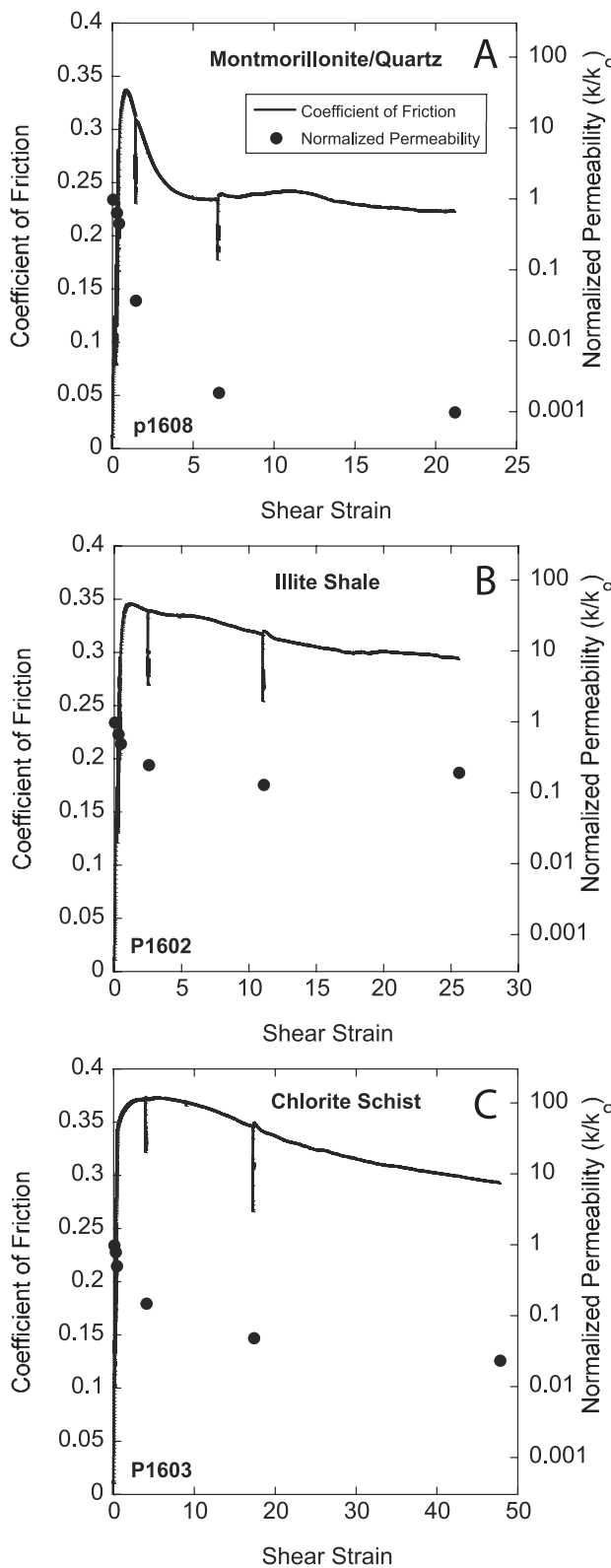


Figure 14. Normalized permeability and coefficient of friction as a function of shear strain for (a) montmorillonite-rich, (b) illite-rich, and (c) chlorite-rich gouges. Permeability values are normalized to the preshear permeability value k_o .

temperature and an effective stress range of 25–75 MPa, they observe permeabilities of $\sim 6 \times 10^{-21}$ to $8 \times 10^{-20} \text{ m}^2$, which are similar to values we report for illite shale at effective normal stresses of 25–58 MPa. Faulkner and Rutter [2003] also observed a trend of decreasing permeability with increasing effective stress. Kwon et al. [2004] observed very low permeability in intact illite shale at effective stresses ranging from 2–10.5 MPa ($2 \times 10^{-20} \text{ m}^2$ to $3 \times 10^{-22} \text{ m}^2$). These values are similar to values we observe in powdered illite shale at high effective normal stress ($5.8 \times 10^{-20} \text{ m}^2$); we attribute the higher permeability we observe at lower effective normal stress to the non-cohesive nature of our samples.

[29] Morrow et al. [1984] report permeabilities for granular samples of pure montmorillonite, pure illite, and a chlorite-rich fault rock. The highest permeability values they report are $\sim 7 \times 10^{-21} \text{ m}^2$ for montmorillonite gouge, $\sim 6 \times 10^{-20} \text{ m}^2$ for illite gouge, and $\sim 3 \times 10^{-19} \text{ m}^2$ for chlorite gouge in triaxial compression with confining pressures of 5 to 10 MPa. These values are significantly lower than the permeability we observe, however we attribute this to the purity of the montmorillonite and illite samples in their experiments. Morrow et al. [1984] also observed permeability reduction as a result of shear, in general agreement with our observations. However, the magnitude of permeability reduction was significantly smaller for illite (~ 0.5 orders of magnitude) and montmorillonite (~ 0.2 orders of magnitude) than in our experiments, which may be the result of lower strains (≤ 10) in their experiments compared to ours.

4.2. Mechanisms of Observed Hydromechanical Behavior

[30] The observed frictional behavior for all the gouges in this study indicates that under the conditions we investigated, faults with these clay compositions are frictionally weak and are not candidates for seismic nucleation. The fact that clay minerals are common in major active fault zones, combined with the observation that clay minerals generally slide stably at normal stress conditions relevant to typical depths of earthquake nucleation, suggests that factors other than clay composition are likely to control the up-dip limit of the seismogenic zone. The consistent velocity-strengthening nature of clay-rich fault gouges may be attributed to the characteristic velocity-strengthening behavior of granular, noncohesive gouge [e.g., Marone and Scholz, 1988]. This behavior may be accentuated by dilation-driven transient depressurization of pore fluid with increased sliding velocity, which would increase the effective normal stress.

[31] The purely frictional component of gouge behavior may be analyzed within the context of nominally room-dry experimental work by detailed examination of individual frictional constitutive parameters a and b . The contribution of transient pore fluid depressurization to the velocity-strengthening behavior of fault gouge is only manifested in fluid-saturated gouge; under these conditions in clay-rich gouge, decoupling of pure frictional effects from poroelastic effects is not straightforward, because water likely affects both the surface properties of clays (and thus frictional behavior of grain contacts) and also mediates transient changes in shear strength via its effects on effective normal stress [e.g., Moore and Lockner, 2004; Samuelson et al.,

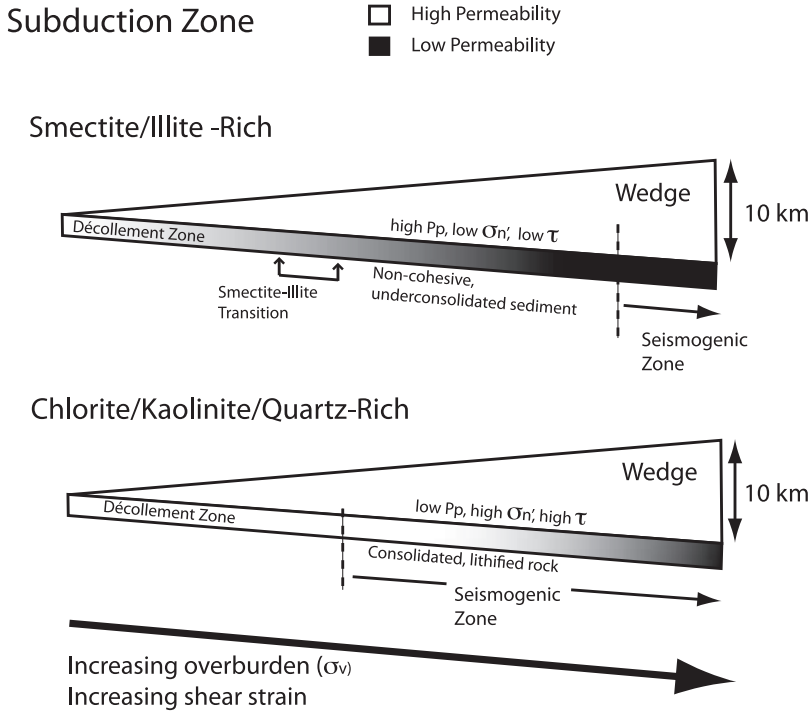


Figure 15. Model illustrating the possible geologic effects of low-permeability and high-permeability sediments in subduction zone megathrusts. For both wedges, the aseismic zone is associated with unlithified sediments and high pore pressure, low effective normal stress, and low shear stress in the décollement, while the seismogenic zone is associated with lithified fault rock, low pore pressure, high effective normal stress, and high shear stress. Basal dip angle is assumed to be 5° , overburden stress gradient is assumed to be ~ 20 MPa/km.

2006, 2007]. However, because both frictional and poroelastic mechanisms act to enhance velocity-strengthening, detailed quantification of their relative contributions is probably less important than characterizing their combined net effect on macroscopic fault behavior. However, it is important to note that transient pore fluid effects are highly dependent on gouge permeability, which implies that gouge permeability may have a significant impact on frictional stability [e.g., Segall and Rice, 1995; Samuelson et al., 2006, 2007].

4.2.1. Frictional Behavior

[32] The values of the friction constitutive parameter a we observe are similar to those observed by Saffer and Marone [2003] for undersaturated montmorillonite-rich and illite-rich gouges. Thus the higher $a - b$ values observed in this study are attributable to lower values of b . Previous studies have interpreted the physical significance of b to be a measure of frictional strength change due to evolution of contact surfaces [Dieterich, 1979, 1981; Scholz, 2002]. At low velocities, values of b approaching 0 are consistent with the idea of “contact saturation” in which mineral surfaces are in complete contact, and therefore the real area of contact does not evolve when the velocity is perturbed [Saffer and Marone, 2003]. This is most likely to occur in phyllosilicates because of (1) their characteristic platy structure, (2) their high grain compressibility, and (3) the increased tendency of phyllosilicate gouges to readily compact and align, especially when saturated with fluid.

[33] Negative values of b , or in some cases b_2 where a second state variable is required, have been reported previously for gabbro at room temperature [Marone and Cox, 1994] and for granular quartz and granite at elevated temperature [Karner et al., 1997; Blanpied et al., 1998]. Values of b approaching 0 have been observed in frictional studies involving other weak minerals such as serpentine [Reinen et al., 1991] and talc [Moore and Lockner, 2008]. Additionally, Chester and Higgs [1992] found that a value of $b = 0$ provided the best fit for modeling data from high temperature ultrafine quartz experiments in which dissolution-precipitation mechanisms are active. Microstructural observations from the Chester and Higgs [1992] experiments indicated almost a complete loss of porosity, suggesting contact saturation.

[34] Contact saturation would also lead to normal stress-independent shear strength, as observed by Saffer and Marone [2003], who noted a coincidence of b values near zero, and the onset of decreasing pressure dependence of shear strength at effective normal stresses $\gtrsim 40$ MPa. Our results are consistent with this hypothesis, in that we observe both low dependence of shear stress on effective normal stress, and b values near zero throughout the range of effective normal stress we investigated. The occurrence of low normal stress-dependent shear strength (or, alternatively, rollover in friction envelope) at low effective normal stress in our study is similar to that observed by Saffer and Marone [2003] and Ikari et al. [2007]. At high velocities, occurrence of $b = 0$ and the negative rate dependence of b

may occur because contact lifetime is sufficiently small that any time-dependent strengthening effects are negligible.

[35] Our constitutive modeling also indicates some negative values of b , which are more difficult to interpret (Figure 5). The fact that values of both a and D_c for velocity steps with negative b are similar to those with a positive b seems to validate the existence of significantly negative values of b . However, if we interpret a value of $b = 0$ to signify saturation of contact area, then negative values of b (evolution to a higher shear strength) cannot be associated with a further increase in contact area. In fact, our observation of dilatancy during velocity steps would seem to indicate the opposite. We propose two possible explanations that may cause the observation of negative values of b , one a pure mechanical effect, the second requiring operation of pore fluid. The first (mechanical) explanation is that during a velocity increase, shear stress may transiently increase due to a dilatant mechanism unrelated to porosity. This might be accomplished by macroscopic gouge layer deformation via the formation of small-scale “kink” structures [Mares and Kronenberg, 1993]. In this case, the aggregate expansion from either kink formation or crystal deformation would thus be observable as dilation of the gouge layer, and would occur over the characteristic displacement D_c . We caution that this mechanism for a negative b , while plausible, is highly speculative. The second explanation for negative b requires transient changes in pore fluid pressure, which we explore in the next section.

4.2.2. Effects of Transient Pore Pressure on Friction

[36] In fluid saturated fault gouge, transient changes in pore fluid pressure may have a significant effect on friction if the layer is unable to efficiently drain. This is likely in sheared, clay-rich fault gouge in which the permeability is extremely low [e.g., Segall and Rice, 1995]. Immediately following a velocity step, we consistently observe positive dilation, indicating an increase in pore volume. This should result in a local reduction of pore fluid pressure, which would in turn cause a local increase in effective normal stress. Normal stress-stepping experiments [Linker and Dieterich, 1992; Richardson and Marone, 1999; Boettcher and Marone, 2004; Hong and Marone, 2005] have shown that the shape of the frictional response to a normal stress step is described by a linear increase, followed by a positive logarithmic decay to a steady state value. Qualitatively this is the same as our observed frictional response to a velocity step when b is negative (e.g., Figure 5).

[37] Transient decreases in pore pressure will be observable as an increase in shear stress if pore fluid is unable to diffuse into the layer over the duration of the velocity steps, which range from 2.67–800 s in our study. The time necessary for fluid pressure to reequilibrate after a perturbation can be estimated from a characteristic diffusion time t :

$$t = \frac{h^2 S}{2\kappa} \quad (9)$$

Where h is the layer thickness, and (κ/S) is the hydraulic diffusivity (m^2/s), where κ is hydraulic conductivity (m/s) and S is specific storage (m^{-1}). Specific storage is given by: $S = \gamma_w(\beta_p + \phi\beta_w)$, where γ_w is the specific weight of water (N/m^3), β_p is the compressibility of the porous matrix (m^2/N), β_w is the compressibility of water (m^2/N),

and ϕ is fractional porosity. In equation (9), we use the full layer thickness, which represents the maximum distance between a potential location of pore fluid perturbation and the controlling reservoir. Assuming that water is much less compressible than the clay gouge and that the porosity is low, the term $\phi\beta_w$ can be neglected. Substituting into equation (9) and rewriting κ in terms of intrinsic permeability and fluid viscosity yields an expression for the characteristic diffusion time:

$$t = \frac{h^2 \beta_p \eta}{2k} \quad (10)$$

Assuming that the compressibility of our gouge layers falls within the range of plastic clay ($2.1 \times 10^{-6} \text{ m}^2/\text{N}$) and medium hard clay ($6.9 \times 10^{-8} \text{ m}^2/\text{N}$ [Domenico and Mifflin, 1965]), the calculated characteristic diffusion times of most of our gouge layers is longer than the duration of the longest velocity step (800 s), especially for gouges with permeability less than $1 \times 10^{-18} \text{ m}^2$ (montmorillonite, illite). However, our observation of minimal excess pore pressure development downstream (P_{p_b}) suggest that this is a small effect if present at all, likely because the actively dilating zone within the gouge layer is very thin, such that the path length for fluid pressure diffusion in equation (10) is considerably smaller than our assumed value of h . Nevertheless, we cannot rule out the possibility that transient depressurization of pore fluid may contribute to the observed velocity-strengthening behavior.

[38] Although transient pore pressure reduction may contribute to the observed velocity-strengthening behavior, we emphasize that it is unlikely to act as the sole cause of low to negative values of b . For instance, high permeability gouge such as chlorite at 12 MPa effective normal stress has a calculated characteristic diffusion time of 0.2–5.6 s. This is sufficient time for any pore pressure deficit to be replenished at all except possibly the highest slip velocity, however b is negative over the entire velocity range. Additionally, in extremely low permeability gouge such as montmorillonite, at effective normal stresses of >25 MPa, positive values of b are still observed despite the fact that equilibration times determined from equation (10) are considerably longer than the duration of the velocity step. These observations indicate that the strongly positive rate dependence of clay-rich gouge is primarily a result of inherent frictional characteristics of the gouge, and that transient fluid depressurization probably plays a secondary role. Based on our data, we cannot definitively determine the relative importance of these processes, but because the two effects are complementary rather than competing, we consider their combined net effect on shear strength (as measured in our experiments) to be the most relevant to macroscopic fault behavior. If transient depressurization of pore fluid is in fact a significant contributor to velocity-strengthening behavior, then gouge permeability likely plays an important role in fault stability. We anticipate that its effect will be amplified if the pore pressure is high relative to the effective normal stress.

4.2.3. Permeability and Pore Pressure

[39] The low permeability observed in clay-rich fault gouge, especially in montmorillonite-rich and illite-rich gouge, is not surprising, nor is the reduction in permeability

as a result of shearing and increased effective stress [e.g., *Arch and Maltman*, 1990; *Crawford et al.*, 2008]. We note that most of the permeability reduction during shearing occurs at low shear strains for all three gouge materials (<5, Figure 14). This permeability decrease occurs over the same range of shear strains as the attainment of residual friction, which is consistent with the idea that fabric development is the underlying cause of both observations [*Haines et al.*, 2009].

[40] Numerical modeling studies have shown that overpressures within fault zones can be generated by either (1) a source of fluids at the root of the fault, combined with sufficient permeability anisotropy (3–5 orders of magnitude) such that the fault acts as a fluid conduit parallel to the structure and barrier normal to it [e.g., *Rice*, 1992], or (2) a source of fluid internal to the fault, combined with low overall permeability [e.g., *Sleep and Blanpied*, 1992; *Miller et al.*, 1996]. Some experimental results show that in sheared phyllosilicate gouges, permeability is reduced both normal and parallel to the fault plane, which can cause permeability anisotropy of up to 3 orders of magnitude [*Faulkner and Rutter*, 1998] but usually lower than 2 orders of magnitude [*Brown and Moore*, 1993; *Dewhurst et al.*, 1996; *Zhang et al.*, 1999, 2001]. However, high pore pressures may still be generated and maintained if overall permeability is sufficiently low. Based on our experimental results, the potential magnitude of pore pressure developed by these mechanisms is likely to depend on gouge mineralogy.

[41] The hydrologic properties of our chlorite gouge are also intriguing in their difference from montmorillonite and illite gouges. Not only does the chlorite gouge exhibit consistently higher permeability than the montmorillonite and illite gouges under all of our experimental conditions, but shearing does not reduce the chlorite gouge permeability as much as in the other gouges. This most likely results from the larger average grain size of the chlorite gouge; this result may still be relevant to natural faults, because chlorite is formed at higher pressure and temperature conditions than montmorillonite and illite, and thus detrital chlorite may be more likely to remain as larger aggregates within natural shear zones.

4.3. Application to Natural Fault Zones

[42] Based on our experimental results, we suggest a conceptual model for the effects of permeability and frictional constitutive properties on macroscopic fault behavior, using subduction thrusts as an example (Figure 15). We illustrate the difference between a low permeability gouge dominated by smectite or illite, and a high permeability gouge dominated by minerals such as chlorite or quartz or kaolinite, which have similar strength and permeability to chlorite [*Crawford et al.*, 2008]. Both net shear strain and the vertical overburden stress σ_v are expected to increase downdip along the thrust plane. Due to the similar permeability and frictional velocity dependence of montmorillonite and illite gouges, the smectite-illite transition is not expected to significantly affect permeability or sliding stability [e.g., *Saffer and Marone*, 2003; *Brown et al.*, 2003]. Montmorillonite or illite gouges, however, have sufficiently low permeability that elevated pore pressures are likely and would significantly lower the effective normal

stress and shear strength. This may potentially explain both the low inferred shear stresses along strike-slip faults (such as the San Andreas [e.g., *Hickman*, 1991]) and subduction thrusts [*Wang and He*, 1999].

[43] In contrast, based on the modest permeability reduction at shear strains of above ~10, our results indicate that chlorite-rich or quartz-rich gouges could maintain their high permeability to significant depth. This would limit their potential to develop high pore pressures, leading to higher effective normal stress, which in turn increases the tendency for unstable slip [e.g., *Scholz*, 1998]. Lower overall pore pressure may also reduce potential velocity strengthening from dilatancy-driven transient pore pressure reduction. Moreover, lower overall pore pressure would facilitate consolidation and lithification of gouge, processes hypothesized to govern the upper aseismic-seismic transition (the “updip limit” [*Marone and Scholz*, 1988; *Moore and Saffer*, 2001, 2007; *Moore et al.*, 2007]). This suggests that the upper transition from aseismic slip to the seismogenic zone should occur shallower along a high-permeability décollement than along a low-permeability one (Figure 15 [e.g., *Saffer and Bekins*, 2006]).

[44] Our experimental results indicate that noncohesive, unlithified sediment may be inherently velocity strengthening, because the frictional contact saturation thought to cause extremely low (or negative) values of b is predominant in unlithified gouge at low temperature. Thus we argue that increasing normal stress and total accumulated shear strain in the fault slip direction alone are insufficient to cause fault instability, and that the transition to seismic slip may require processes such as gouge lithification via consolidation, cementation, mineral diagenesis, and dissolution-precipitation reactions [*Marone and Scholz*, 1988; *Moore and Saffer*, 2001, 2007; *Moore et al.*, 2007]. These processes become increasingly active at higher temperatures, and thus are expected to have a larger effect with increasing depth. Support for this hypothesis comes from numerous rock mechanics studies showing that velocity-weakening behavior (large values of b , exceeding a) is observed in intact, initially bare rock-on-rock granite experiments [e.g., *Dieterich*, 1979; *Tullis and Weeks*, 1986]. Velocity-weakening behavior has also been observed in granular fault gouge in which shear localization has occurred, causing the gouge behavior to be similar to that in rock-on-rock experiments [*Beeler et al.*, 1996; *Scruggs and Tullis*, 1998; *Niemeijer and Spiers*, 2005]. In localized shear of lithified or semolithified rock, individual grains are prevented from arranging to a state of maximum contact area, resulting in values of $b > a$ and thus leading to velocity weakening.

[45] Because the constitutive parameter a is always positive, values of $b \leq 0$ guarantee velocity-strengthening behavior. Modeling of the temporal distribution of aseismic creep events, such as earthquake afterslip, using spring slider models typically requires velocity-strengthening friction [e.g., *Marone et al.*, 1991]. *Perfettini and Avouac* [2004] modeled postseismic slip following the 1999 Chi-Chi earthquake in Taiwan using a rate-dependent model only, which is essentially a rate-dependent and state-dependent model in which $b = 0$. Additionally, *Savage and Langbein* [2008] recently modeled postseismic relaxation following the 2004 Parkfield, California earthquake. They found that afterslip

was satisfactorily modeled using both rate-only and rate-dependent and state-dependent friction but that the rate-dependent and state-dependent models required b to be negative. Our finding that the constitutive parameter b is in fact ≤ 0 over a relevant range of effective normal stress and slip velocities provides the first direct laboratory constraint for realistic fault zone materials that supports these models, especially when considering faults with abundant clay minerals.

5. Conclusions

[46] We performed laboratory experiments on water-saturated clay-rich fault gouges containing montmorillonite, illite, and chlorite at effective normal stresses up to 59 MPa. Our results indicate that these clay-rich gouges are consistently weak, with a coefficient of friction of <0.35 . Montmorillonite gouge is consistently the weakest gouge, with $\mu = 0.19\text{--}0.23$. All of the gouges we investigated are velocity-strengthening (stably sliding) over the range of conditions we explored. The velocity-strengthening behavior we observe may be characteristic of noncohesive, unlithified phyllosilicate gouge material caused by low values of the friction constitutive parameter b .

[47] Permeability measurements of clay-rich gouge indicate that shearing significantly reduces cross-fault permeability. Montmorillonite and illite gouges are consistently the least permeable, whereas chlorite gouge is the most permeable and also maintains a higher permeability after shearing. This characteristic may be significant in that the presence or formation of chlorite may allow drainage, thus reducing pore pressure and allowing increased effective stress in the fault zone. Because high pore pressure hinders processes such as consolidation and cementation, low pore pressure and high effective stress may increase the likelihood for seismic nucleation if fault instability is indeed linked to cohesive strengthening and lithification.

[48] **Acknowledgments.** We thank André Niemeijer for comments on the manuscript and aid in the laboratory and Mike Underwood for XRD work. Constructive reviews by Dan Faulkner, Sheryl Tembe, and an anonymous reviewer are greatly appreciated. This work was supported by NSF grant OCE-0648331 to C. Marone and D.M. Saffer, and acknowledgment is made to the Donors of the American Chemical Society Petroleum Research Fund for partial support of this research.

References

- Arch, J., and A. Maltman (1990), Anisotropic permeability and tortuosity in deformed wet sediments, *J. Geophys. Res.*, **95**, 9035–9045.
- Beeler, N. M., T. E. Tullis, and M. L. Blanpied (1996), Frictional behavior of large displacement experimental faults, *J. Geophys. Res.*, **101**, 8697–8715.
- Bizzari, A., and M. Cocco (2006a), A thermal pressurization model for the spontaneous dynamic rupture propagation on a three-dimensional fault: 1. Methodological approach, *J. Geophys. Res.*, **111**, B05303, doi:10.1029/2005JB003862.
- Bizzari, A., and M. Cocco (2006b), A thermal pressurization model for the spontaneous dynamic rupture propagation on a three-dimensional fault: 2. Traction evolution and dynamic parameters, *J. Geophys. Res.*, **111**, B05304, doi:10.1029/2005JB003864.
- Blanpied, M. L., C. J. Marone, D. A. Lockner, J. D. Byerlee, and D. P. King (1998), Quantitative measure of the variation in fault rheology due to fluid-rock interactions, *J. Geophys. Res.*, **103**, 9691–9712.
- Boettcher, M. S., and C. Marone (2004), Effects of normal stress variation on the strength and stability of creeping faults, *J. Geophys. Res.*, **109**, B03406, doi:10.1029/2003JB002824.
- Bourlange, S., L. Jounioux, and P. Henry (2004), Data report: Permeability, compressibility, and friction coefficient measurements under confining pressure and strain, Leg 190, Nankai Trough, in *Proc. ODP Sci. Results, 190/196*, edited by H. Mikada et al., pp. 1–16, College Station, Tex. (Ocean Drilling), doi:10.2973/odp.proc.sr.190196.215.2004.
- Brown, K. M., and J. C. Moore (1993), Comment on “Anisotropic permeability and tortuosity in deformed wet sediments” by J. Arch and A. Maltman, *J. Geophys. Res.*, **98**, 17,859–17,864.
- Brown, K. M., A. Kopf, M. B. Underwood, and J. L. Weinberger (2003), Compositional and fluid pressure controls on the state of stress on the Nankai subduction thrust: A weak plate boundary, *Earth Planet. Sci. Lett.*, **214**, 589–603.
- Byerlee, J. (1990), Friction, overpressure, and fault normal compression, *Geophys. Res. Lett.*, **17**, 2109–2112.
- Byerlee, J. D. (1978), Friction of rocks, *Pure Appl. Geophys.*, **116**, 215–626.
- Byrne, T., and D. Fisher (1990), Evidence for a weak and overpressured décollement beneath sediment-dominated accretionary prisms, *J. Geophys. Res.*, **95**, 9081–9097.
- Chester, F. M., and N. G. Higgs (1992), Multimechanism friction constitutive model for ultrafine quartz gouge at hypocentral locations, *J. Geophys. Res.*, **97**, 1859–1870.
- Crawford, B. R., D. R. Faulkner, and E. H. Rutter (2008), Strength, porosity, and permeability development during hydrostatic and shear loading of synthetic quartz-clay fault gouge, *J. Geophys. Res.*, **113**, B03207, doi:10.1029/2006JB004634.
- Davis, D., J. Suppe, and F. A. Dahlen (1983), Mechanics of fold-and-thrust belts and accretionary wedges, *J. Geophys. Res.*, **88**, 1153–1172.
- Deng, X., and M. B. Underwood (2001), Abundance of smectite and the location of a plate-boundary fault, Barbados accretionary prism, *Geol. Soc. Am. Bull.*, **113**, 495–507.
- Dewhurst, D. N., K. M. Brown, M. B. Clennell, and G. K. Westbrook (1996), A comparison of the fabric and permeability anisotropy of consolidated and sheared silty clay, *Eng. Geol.*, **42**, 253–267.
- Dieterich, J. H. (1979), Modeling of rock friction: 1. Experimental results and constitutive equations, *J. Geophys. Res.*, **84**, 2161–2168.
- Dieterich, J. H. (1981), Constitutive properties of faults with simulated gouge, in *Mechanical Behavior of Crustal Rocks*, *Geophys. Monogr. Ser.*, vol. 24, edited by N. L. Carter et al., pp. 102–120, AGU, Washington, D. C.
- Dieterich, J. H., and B. Kilgore (1996), Implications of fault constitutive properties for earthquake prediction, *Proc. Natl. Acad. Sci.*, **93**, 3787–3794.
- Domenico, P. A., and M. D. Mifflin (1965), Water from low-permeability sediments and land subsidence, *Water Resources Res.*, **1**, 563–576.
- Faulkner, D. R., and E. H. Rutter (1998), The gas permeability of clay-bearing fault gouge at 20°C, in *Faults, Fault Sealing and Fluid Flow in Hydrocarbon Reservoirs*, edited by G. Jones, Q. Fisher, and R. J. Knipe, *Geol. Soc. Spec. Publ.*, **147**, 147–156.
- Faulkner, D. R., and E. H. Rutter (2000), Comparisons of water and argon permeability in natural clay-bearing fault gouge under high pressure at 20°C, *J. Geophys. Res.*, **105**, 16,415–16,426.
- Faulkner, D. R., and E. H. Rutter (2001), Can the maintenance of overpressured fluids in large strike-slip fault zones explain their apparent weakness?, *J. Geophys. Res.*, **29**, 503–506.
- Faulkner, D. R., and E. H. Rutter (2003), The effect of temperature, the nature of the pore fluid, and subyield differential stress on the permeability of phyllosilicate-rich fault gouge, *J. Geophys. Res.*, **108**(B5), 2227, doi:10.1029/2001JB001581.
- Haines, S. H., B. A. van der Pluijm, M. J. Ikari, D. M. Saffer, and C. Marone (2009), Clay fabrics in natural and artificial gouge, *J. Geophys. Res.*, doi:10.1029/2008JB005866, in press.
- Handin, J. (1969), On the Coulomb-Mohr failure criterion, *J. Geophys. Res.*, **74**, 5343–5348.
- Hickman, S. H. (1991), Stress in the lithosphere and the strength of active faults, *Rev. Geophys.*, pp. 759–775, U.S. Natl. Rep. to Int. Union of Geodesy and Geophysics.
- Hong, T., and C. Marone (2005), Effects of normal stress perturbations on the frictional properties of simulated faults, *Geochem. Geophys. Geosyst.*, **6**, Q03012, doi:10.1029/2004GC000821.
- Hubbert, M. K., and W. W. Rubey (1959), Role of fluid pressure in mechanics of overthrust faulting: 1. Mechanics of fluid-filled porous solids, and its application to overthrust faulting, *GSA Bull.*, **70**, 115–166.
- Hyndman, R. D., M. Yamano, and D. A. Oleskevich (1997), The seismogenic zone of subduction thrust faults, in *The Island Arc*, vol. 6, pp. 244–260.
- Ikari, M. J., D. M. Saffer, and C. Marone (2007), Effect of hydration state on the frictional properties of montmorillonite-based fault gouge, *J. Geophys. Res.*, **112**, B06423, doi:10.1029/2006JB004748.
- Karner, S. L., C. Marone, and B. Evans (1997), Laboratory study of fault healing and lithification in simulated fault gouge under hydrothermal conditions, *Tectonophysics*, **277**, 41–55.
- Kopf, A., and K. M. Brown (2003), Friction experiments on saturated sediments and their implications for the stress state of the Nankai and Barbados subduction thrusts, *Mar. Geol.*, **202**, 193–210.

- Kwon, O., A. K. Kronenberg, A. F. Gangi, B. Johnson, and B. E. Herbert (2004), Permeability of illite-bearing shale: 1. Anisotropy and effects of clay content and loading, *J. Geophys. Res.*, **109**, B10205, doi:10.1029/2004JB003052.
- Le Pichon, X., P. Henry, and S. Lallemand (1993), Accretion and erosion in subduction zones: The role of fluids, *Annu. Rev. Earth Planet. Sci.*, **21**, 307–331.
- Linker, M. F., and J. H. Dieterich (1992), Effects of variable normal stress on rock friction: Observations and constitutive equations, *J. Geophys. Res.*, **97**, 4923–4940.
- Liu, Y., and J. R. Rice (2005), Aseismic slip transients emerge spontaneously in three-dimensional rate and state modeling of subduction earthquake sequences, *J. Geophys. Res.*, **110**, B08397, doi:10.1029/2004JB003424.
- Logan, J. M., and K. A. Rauenzahn (1987), Frictional dependence of gouge mixtures of quartz and montmorillonite on velocity, composition, and fabric, *Tectonophysics*, **144**, 87–108.
- Mares, V. M., and A. K. Kronenberg (1993), Experimental deformation of muscovite, *J. Struct. Geol.*, **15**, 1061–1075.
- Marone, C. (1998), Laboratory-derived friction laws and their application to seismic faulting, *Annu. Rev. Earth Planet. Sci.*, **26**, 643–696.
- Marone, C., and S. J. D. Cox (1994), Scaling of rock friction constitutive parameters: The effects of surface roughness and cumulative offset on friction of gabbro, *Pure Appl. Geophys.*, **143**, 359–385.
- Marone, C., and B. Kilgore (1993), Scaling of the critical slip distance for seismic faulting with shear strain in fault zones, *Nature*, **362**, 618–621.
- Marone, C., and D. M. Saffer (2007), Fault friction and the upper transition from seismic to aseismic faulting, in *The Seismogenic Zone of Subduction Thrust Faults*, edited by T. H. Dixon and J. C. Moore, Columbia Univ. Press, New York.
- Marone, C., and C. H. Scholz (1988), The depth of seismic faulting and the upper transition from stable to unstable slip regimes, *Geophys. Res. Lett.*, **15**, 621–624.
- Marone, C., C. B. Raleigh, and C. H. Scholz (1990), Frictional behavior and constitutive modeling of simulated fault gouge, *J. Geophys. Res.*, **95**, 7007–7025.
- Marone, C., C. H. Scholz, and R. Bilham (1991), On the mechanics of earthquake afterslip, *J. Geophys. Res.*, **96**, 8441–8452.
- Miller, S. A., A. Nur, and D. L. Olgaard (1996), Earthquakes as a coupled shear stress—high pore pressure dynamical system, *Geophys. Res. Lett.*, **23**, 197–200.
- Moore, D. E., and D. A. Lockner (2004), Crystallographic controls on the frictional behavior of dry and water-saturated sheet structure minerals, *J. Geophys. Res.*, **109**, B03401, doi:10.1029/2003JB002582.
- Moore, D. E., and D. A. Lockner (2008), Talc friction in the temperature range 25°C–400°C: Relevance for fault zone weakening, *Tectonophysics*, **449**, 120–132.
- Moore, J. C., and D. M. Saffer (2001), Updip limit of the seismogenic zone beneath the accretionary prism of Southwest Japan: An effect of diagenetic to low-grade metamorphic processes and increasing effective stress, *Geology*, **29**, 183–186.
- Moore, J. C., C. Rowe, and F. Meneghini (2007), How accretionary prisms elucidate seismogenesis in subduction zones, in *The Seismogenic Zone of Subduction Thrust Faults*, edited by T. H. Dixon and J. C. Moore, Columbia Univ. Press, New York.
- Morrow, C. A., L. Q. Shi, and J. D. Byerlee (1984), Permeability of fault gouge under confining pressure and shear stress, *J. Geophys. Res.*, **89**, 3193–3200.
- Morrow, C., B. Radney, and J. Byerlee (1992), Frictional strength and the effective pressure law of montmorillonite and illite clays, in *Fault Mechanics and Transport Properties of Rocks*, edited by B. Evans and T.-F. Wong, pp. 69–88, Academic Press, Ltd., San Diego, Calif.
- Morrow, C. A., D. E. Moore, and D. A. Lockner (2000), The effect of mineral bond strength and adsorbed water on fault gouge frictional strength, *Geophys. Res. Lett.*, **27**, 815–818.
- Niemeijer, A. R., and C. J. Spiers (2005), Influence of phyllosilicates on fault strength in the brittle-ductile transition: Insights from rock analogue experiments, in *High-Strain Zones: Structure and Physical Properties*, edited by D. Bruhn and L. Burlini, *Geol. Soc. Lond. Spec. Publ.*, **245**, 303–327.
- Noda, H., and T. Shimamoto (2005), Thermal pressurization and slip-weakening distance of a fault: An example of the Hanaore fault, southwest Japan, *Bull. Seismol. Soc. Am.*, **95**, 1224–1233, doi:10.1785/0120040089.
- Numelin, T., C. Marone, and E. Kirby (2007), Frictional properties of natural fault gouge from a low-angle normal fault, Panamint Valley, California, *Tectonics*, **26**, TC2004, doi:10.1029/2005TC001916.
- Perfettini, H., and J.-P. Avouac (2004), Postseismic relaxation driven by brittle creep: A possible mechanism to reconcile geodetic measurements and the decay rate of aftershocks, application to the Chi-Chi earthquake, Taiwan, *J. Geophys. Res.*, **109**, B02304, doi:10.1029/2003JB002488.
- Reinen, L. A., and J. D. Weeks (1993), Determination of rock friction constitutive parameters using an iterative least-squares inversion method, *J. Geophys. Res.*, **98**, 15,937–15,950.
- Reinen, L. A., J. D. Weeks, and T. E. Tullis (1991), The frictional behavior of serpentinite: Implications for aseismic creep on shallow crustal faults, *Geophys. Res. Lett.*, **18**, 1921–1924.
- Richardson, E., and C. Marone (1999), Effects of normal stress vibrations on frictional healing, *J. Geophys. Res.*, **104**, 28,859–28,878.
- Rice, J. R. (1992), Fault stress states, pore pressure distributions, and the weakness of the San Andreas Fault, in *Fault Mechanics and Transport Properties of Rocks*, edited by B. Evans and T.-F. Wong, pp. 475–503, Academic Press, Ltd., San Diego, Calif.
- Rice, J. R. (2006), Heating and weakening of faults during earthquake slip, *J. Geophys. Res.*, **111**, B05311, doi:10.1029/2005JB004006.
- Rubin, A. M. (2008), Episodic slow slip events and rate-and-state friction, *J. Geophys. Res.*, **113**, B11414, doi:10.1029/2008JB005642.
- Saffer, D. M., and B. A. Bekins (2006), An evaluation of factors influencing pore pressure in accretionary complexes: Implications for taper angle and wedge mechanics, *J. Geophys. Res.*, **111**, B04101, doi:10.1029/2005JB003990.
- Saffer, D. M., and C. Marone (2003), Comparison of smectite- and illite-rich gouge frictional properties: Application to the updip limit of the seismogenic zone along subduction megathrusts, *Earth Planet. Sci. Lett.*, **215**, 219–235.
- Samuelson, J., C. Marone, and D. Elsworth (2006), The effect of dilatancy and compaction on the stability and permeability of a fluid-infiltrated fault, *Eos Trans. AGU*, **87**(52), Fall Meet. Suppl., Abstract S33A-0218.
- Samuelson, J., C. Marone, and D. Elsworth (2007), Hydro-mechanical processes in faulting: An experimental analysis of the variability of dilatancy in simulated fault gouge, *Eos Trans. AGU*, **88**(52), Fall Meet. Suppl., Abstract T42-C-07.
- Savage, J. C., and J. Langbein (2008), Postearthquake relaxation after the 2004 M6 Parkfield, California, earthquake and rate-and-state friction, *J. Geophys. Res.*, **113**, B10407, doi:10.1029/2008JB005723.
- Scholz, C. H. (1998), Earthquakes and friction laws, *Nature*, **391**, 38–42.
- Scholz, C. H. (2002), *The Mechanics of Earthquakes and Faulting*, 2nd ed., Cambridge Press, New York.
- Scruggs, V. J., and T. E. Tullis (1998), Correlation between velocity dependence of friction and strain localization in large displacement experiments on feldspar, muscovite and biotite gouge, *Tectonophysics*, **295**, 15–40.
- Segall, P., and J. R. Rice (1995), Dilatancy, compaction, and slip instability of a fluid-infiltrated fault, *J. Geophys. Res.*, **100**, 22,155–22,171.
- Segall, P., and J. R. Rice (2006), Does shear heating of pore fluid contribute to earthquake nucleation?, *J. Geophys. Res.*, **111**, B09316, doi:10.1029/2005JB004129.
- Shimamoto, T., and J. M. Logan (1981), Effects of simulated clay gouges on the sliding behavior of Tennessee sandstone, *Tectonophysics*, **75**, 243–255.
- Sleep, N. H., and M. L. Blanpied (1992), Creep, compaction and the weak rheology of major faults, *Nature*, **359**, 687–692.
- Takahashi, M., K. Mizoguchi, K. Kitamura, and K. Masuda (2007), Effects of clay content on the frictional strength and fluid transport property of faults, *J. Geophys. Res.*, **112**, B08206, doi:10.1029/2006JB004678.
- Tullis, T. E., and J. D. Weeks (1986), Constitutive behavior and stability of frictional sliding of granite, *Pure Appl. Geophys.*, **124**, 383–414.
- Underwood, M. B. (2007), Sediment inputs to subduction zones: Why lithostratigraphy and clay mineralogy matter, in *The Seismogenic Zone of Subduction Thrust Faults*, edited by T. H. Dixon and J. C. Moore, Columbia Univ. Press, New York.
- Vrolijk, P., and B. A. van der Pluijm (1999), Clay gouge, *J. Struct. Geol.*, **21**, 1039–1048.
- Wang, K., and J. He (1999), Mechanics of low-stress forearcs: Nankai and Cascadia, *J. Geophys. Res.*, **104**, 15,191–15,205.
- Wang, K., and Y. Hu (2006), Accretionary prisms in subduction earthquake cycles: The theory of dynamic Coulomb wedge, *J. Geophys. Res.*, **111**, B06410, doi:10.1029/2005JB004094.
- Wang, C.-Y., and N.-H. Mao (1979), Shearing of saturated clays in rock joints at high confining pressures, *Geophys. Res. Lett.*, **6**, 825–828.
- Wibberley, C. A. J., and T. Shimamoto (2005), Earthquake slip weakening and asperities explained by thermal pressurization, *Nature*, **436**, 689–692, doi:10.1038/nature03901.
- Wiersberg, T., and J. Erzinger (2007), A helium isotope cross-section study through the San Andreas fault at seismogenic depths, *Geochem. Geophys. Geosyst.*, **8**, Q01002, doi:10.1029/2006GC001388.
- Wiersberg, T., and J. Erzinger (2008), Origin and spatial distribution of gas at seismogenic depths of the San Andreas fault from drill-mud gas analysis, *Appl. Geochem.*, **23**, 1675–1690.

- Wu, F. T., L. Blatter, and H. Roberson (1975), Clay gouges in the San Andreas fault system and their possible implications, *Pure Appl. Geophys.*, 113, 87–95.
- Yang, Y., and A. Aplin (2007), Permeability and petrophysical properties of 30 natural mudstones, *J. Geophys. Res.*, 112, B03206, doi:10.1029/2005JB004243.
- Zhang, S., and S. F. Cox (2000), Enhancement of fluid permeability during shear deformation of a synthetic mud, *J. Struct. Geol.*, 22, 1385–1393.
- Zhang, S., T. E. Tullis, and V. J. Scruggs (1999), Permeability anisotropy and pressure dependency of permeability in experimentally sheared gouge materials, *J. Struct. Geol.*, 21, 795–806.
- Zhang, S., T. E. Tullis, and V. J. Scruggs (2001), Implications of permeability and its anisotropy in a mica gouge for pore pressures in fault zones, *Tectonophysics*, 335, 37–50.

M. J. Ikari, C. Marone, and D. M. Saffer, Department of Geosciences, Pennsylvania State University, 536 Deike Building, University Park, PA 16802, USA. (mikari@geosc.psu.edu)